Journal of Hazardous Materials 419 (2021) 126466

Contents lists available at ScienceDirect

Journal of Hazardous Materials

journal homepage: www.elsevier.com/locate/jhazmat

Research Paper

Construction of direct Z-scheme Bi_5O_7I/UiO-66-NH_2 heterojunction photocatalysts for enhanced degradation of ciprofloxacin: Mechanism insight, pathway analysis and toxicity evaluation

Chen Zhao [a,b], Yang Li [a], Hongyu Chu [a], Xi Pan [a], Li Ling [a], Peng Wang [a], Huifen Fu [a], Chong-Chen Wang [a,*], Zhihua Wang [b,*]

[a] Beijing Key Laboratory of Functional Materials for Building Structure and Environment Remediation, Beijing University of Civil Engineering and Architecture, Beijing 100044, China
[b] State Key Laboratory of Chemical Resource Engineering, Beijing University of Chemical Technology, Beijing 100029, China

ARTICLE INFO

Editor: Dr. B. Lee

Keywords:
Bismuth-rich bismuth oxyhalide
Metal-organic frameworks
Photocatalysis
Z-scheme
Ciprofloxacin

ABSTRACT

Direct Z-scheme Bi_5O_7I/UiO-66-NH_2 (denoted as BU-*x*) heterojunction photocatalysts were successfully constructed through ball-milling method. Photocatalytic activities of the as-prepared BU-*x* samples were determined by using a typical fluoroquinolone antibiotic, ciprofloxacin (CIP). All BU-*x* heterojunctions exhibited better CIP removal performances than that of pristine Bi_5O_7I and UiO-66-NH_2 upon exposure to white light irradiation. In comparison, the heterojunction with UiO-66-NH_2 content of 50 wt% (BU-5) showed excellent structural stability and the optimal adsorption-photodegradation efficiency for the CIP removal. The removal efficiency of CIP (10 mg/L) over BU-5 (0.75 g/L) achieved 96.1% within 120 min illumination. Meanwhile, the effect of photocatalyst dosage, pH and inorganic anions were systemically explored. Reactive species trapping experiments, electron spin resonance (ESR) signals, Mott-Schottky measurements and density functional theory (DFT) simulation revealed that the photo-generated holes (h^+), hydroxyl radical (·OH) and superoxide radical ($\cdot O_2^-$) played crucial roles in CIP degradation. This result can be ascribed to that the unique Z-scheme charge transfer configuration retained the excellent redox capacities of Bi_5O_7I and UiO-66-NH_2. Meanwhile, the CIP degradation pathways and the toxicity of various intermediates were subsequently analyzed. This work provided a feasible idea for removing antibiotics by bismuth-rich bismuth oxyhalide/MOF-based heterostructured photocatalysts.

1. Introduction

Ciprofloxacin (CIP) is a broad-spectrum antibiotic belonging to the class of second-generation quinolone antibiotics and is widely used for resistant bacterial diseases (Phoon et al., 2020; Hu et al., 2020a). Nonetheless, CIP cannot be metabolically decomposed entirely, leading to their discharge into environment. Approximately 31 mg/L of CIP has been detected in pharmaceutical wastewater effluent, 14 mg/L in municipal wastewater effluent, 2500 and 14 μg/L in surface water and groundwater respectively (Li et al., 2020b; Kovalakova et al., 2020). This indicates that the current pharmaceutical wastewater treatment plants (WWTPs) are not adequately effective enough to decontamination of CIP. More seriously, CIP is susceptible to induce bacterial resistance with severe bio-toxic effects in certain probiotics even at extremely low concentrations, thus leading to an increased risk to prevention and control of the human disease (Xu et al., 2019). Hence, it is indispensable to exploit an effective method for the elimination of CIP in different aquatic environments.

Photocatalysis is one of the alternate methods for the treatment of wastewater due to the photo-generated electrons and holes can activate H_2O and/or O_2 at ambient conditions to produce reactive oxygen species (e.g., $\cdot O_2^-$, ·OH, H_2O_2, $^1O_2$) to degrade contaminants (Wei et al., 2020; Chen et al., 2021a). But the high recombination rate of photo-generated charge carriers is still the main obstacle for the photocatalyst based on a single component. Therefore, binary heterojunction photocatalyst is more preferred since the existence of built-in electric field at the interface of different components is contributed to promote the spatial separation of photo-generated electron-hole pairs (Wang et al., 2019b; Yi et al., 2021; Zhao et al., 2021a). Lately, the Z-scheme photocatalysts have gained sufficient attraction over conventional type-II

* Corresponding authors.
E-mail addresses: chongchenwang@126.com, wangchongchen@bucea.edu.cn (C.-C. Wang), zhwang@mail.buct.edu.cn (Z. Wang).

https://doi.org/10.1016/j.jhazmat.2021.126466
Received 29 March 2021; Received in revised form 2 June 2021; Accepted 21 June 2021
Available online 24 June 2021

heterojunction photocatalysts owing to the presence of more positive valence and more negative conduction band in Z-scheme system, which is capable to advance the corresponding photocatalytic activity via an accelerated migration of electrons and holes with strong redox ability (Liao et al., 2021; Low et al., 2017). Based on the aforementioned analyses, fabrication of Z-scheme photocatalytic system would be an efficient approach to prevent the recombination of undesirable electron-hole pairs and simultaneously maintained high redox capacities.

Bismuth-rich bismuth oxyhalides ($Bi_xO_yX_z$, X = Cl, Br and I) belong to a new class of photocatalysts with layered structures characterized by $[Bi_2O_2]^{2+}$ and double $[X]^-$ layers (Zhao et al., 2021a; Jin et al., 2017). The charge density surrounding the [Bi-O] layer is higher compared with the double halogen slabs. Thus, a static internal electric field (IEF) can be generated under the influence of polarization of the non-uniform charge distribution, which in turn results in enhancing transfer of electrons and holes. Among these compounds, Bi_5O_7I is a newly synthesized visible-light-responsive photocatalyst (E_g = 2.85–2.98 eV) with a strong photocatalytic activity (Li et al., 2020d; Xu et al., 2020). More importantly, Bi_5O_7I possesses more positive valence band (VB) edge (~3.0 eV vs. NHE) and could supply more active holes to participate in oxidizing organic contaminants. For example, Sun and the co-workers (Sun et al., 2009) firstly fabricated Bi_5O_7I via hydrothermal method and used it to the photocatalytic degradation of acetaldehyde (CH_3CHO) and rhodamine (RhB). However, pristine Bi_5O_7I still has a lot of disadvantages, such as insufficient absorption capacity for visible light, low transport efficiency of photo-generated electron-hole pairs and photo-corrosion phenomenon limit its photocatalytic performance. Furthermore, the layered structure of Bi_5O_7I was inclined to agglomerate during photocatalytic process and resulted in limited active sites with poor affinity towards target pollutants. Therefore, fabricating a heterostructure by incorporating a suitable multifunctional material with Bi_5O_7I is deliberated to be an essential approach to further boost the photocatalytic activity of Bi_5O_7I.

Metal-organic frameworks, because of their larger surface areas, well-organized porous and tunable structures, have been excessively utilized in the field of photocatalysis (Wang et al., 2019b, 2014, 2016, 2020). Unfortunately, the poor conductivity property restrains its actual photocatalytic applications. UiO-66-NH_2 is a zirconium-based MOF, which not only exhibits the outstanding properties same as other MOFs but also displays high chemical, structural and thermostability in aqueous environments. Additionally, the lowest unoccupied molecular orbital (LUMO) of UiO-66-NH_2 (−1.09 to −0.51 eV vs. NHE) is more negative than that of most MOFs (Zhao et al., 2021a; Zhou et al., 2019), suggesting that photo-generated electrons in the LUMO of NH_2-UiO-66 possessed higher reduction abilities (Zhang et al., 2018; Zhao et al., 2018b). As a result, UiO-66-NH_2 is suitable for combining with Bi_5O_7I to construct a Z-scheme photocatalytic reaction system. Therefore, it is expected that UiO-66-NH_2 with porous structure and large specific surface area will provide a dispersive place for layered structure of Bi_5O_7I to prevent them from aggregating, promote its adsorption capacity and ensure that Bi_5O_7I will effectively receive light irradiation. In turn, Bi_5O_7I can improve the photoelectric activity of UiO-66-NH_2. Finally, the close contact and matched band positions between NH_2-UiO-66 and Bi_5O_7I can greatly improve the photocatalytic efficiency by inhibiting the recombination of photo-generated charge carriers.

In the current work, we proposed the preparation efficient Bi_5O_7I/UiO-66-NH_2 Z-scheme heterojunctions through a facile ball-milling method. Various characterization techniques have been employed to study the physicochemical and photoelectric properties. The photocatalytic performance of the as-prepared materials was investigated via white light irradiated decomposition of CIP. Besides, the effect of photocatalyst dosage, initial pH and co-existence of inorganic ions on adsorption-degradation process were systemically studied. Additionally, the enhanced photocatalysis mechanism, CIP degradation pathways and the toxicity of intermediate products were also investigated.

2. Materials and methods

2.1. Preparation of photocatalysts

2.1.1. Preparation of UiO-66-NH_2

The pristine UiO-66-NH_2 was synthesized by using the previously reported solvothermal method with slight modifications (Zhou et al., 2019; Xu et al., 2018). Briefly, a certain amount of 2-aminoterephthalic acid (0.81 g) and $ZrCl_4$ (1.05 g) was prepared in 40.0 mL *N,N'*-dimethylformamide. After that, acetic acid (17.0 mL) was added into the above mixture with ultrasonic processing about 10 min. The obtained suspension was then transferred to a 100.0 mL Teflon-lined stainless--steel autoclave and provided 24 h heating at 120 °C. The mixture was then cooled at room temperature and the resulting solid material was centrifuged and cleaned several times with ultrapure water to remove residual inorganic ions. Finally, the pale yellow UiO-66-NH_2 powders were oven-dried at 60 °C for 12 h.

2.1.2. Preparation of Bi_5O_7I

Bi_5O_7I was fabricated by calcining BiOI precursor in a muffle furnace directly in air (Liu, 2015; Liu et al., 2015) and the BiOI was synthesized by utilizing the co-precipitation method. The detailed procedures were as follows: $Bi(NO_3)_3$•$5H_2O$ (1.94 g) was incorporated into the 30.0 mL glycol and the obtained suspension was then homogenized by providing ultrasonic processing for 30 min. Meanwhile, a certain amount of KI (0.664 g) was added in 30.0 mL ultrapure water, which was then incorporated into the above suspension of $Bi(NO_3)_3$•$5H_2O$ under vigorous stirring for 2 h. Then, the red-colored BiOI solids were collected via filtration, repeated-washing and drying treatments. Subsequently, the BiOI was placed in an alumina crucible and heated at 520 °C with a rate of 3 °C/min in a muffle furnace for 4 h. Upon cooling at ambient temperature, Bi_5O_7I was obtained as a solid powder.

2.1.3. Preparation of UiO-66-NH_2/Bi_5O_7I heterojunctions

As described in Fig. 1, various Bi_5O_7I/UiO-66-NH_2 heterojunctions (BU-*x*) were prepared by ball-milling method. As in standard procedure, 0.10 g of Bi_5O_7I and different amounts of UiO-66-NH_2 (0.01, 0.03, 0.05, 0.07 and 0.09 g) were added into a Nanjing Nanda planet-type milling instrument. The milling mediums were stainless steel balls with 10 mm or 20 mm diameter. The operating frequency and time were set as 30 Hz and 20 min. Then the final products were BU-*x* photocatalysts, weight percentages of 10%, 30%, 50%, 70% and 90% were denoted as BU-1, BU-3, BU-5, BU-7 and BU-9, respectively.

2.2. Material characterizations

Analysis for the crystal structure was conducted by Dandonghaoyuan DX2700B X-ray diffractometer (XRD) using Cu Kα radiation with scan angles ranging from 5° to 60°. The functional group was detected by a Thermo Nicolet 6700 Fourier transform infrared (FT-IR) spectrometer in the range of 4000–400 cm^{-1}. Morphological assessment and characterization of element distribution of the prepared materials were conducted by a Hitachi SU8020 scanning electron microscopy (SEM) and a JEOL JEM-2100F transmission electron microscopy (TEM). The phase compositions including selected area electron diffraction pattern (SAED) were determined by a FEI Tecnai G2 F30 high-resolution transmission electron microscopy (HRTEM). The UV–vis diffuse reflectance spectra (UV–vis DRS) were recorded by a PerkinElmer Lambda 650S spectrophotometer. The valence states of the elements were documented by a ThermoFisher Escalab 250XI X-ray photoelectron spectrometer (XPS) with C 1s to calibrate peak positions. The Brunauer-Emmett-Teller (BET) surface areas of the samples were estimated with the aid of a Micromeritics ASAP 2460 physical absorption analyzer. The steady-state photoluminescence (PL) spectra were measured by a Hitachi F-7000

Fig. 1. The fabrication procedure of the BU-*x* heterojunctions.

fluorescence spectrophotometer with excitation wavelength of 350 nm. Time-resolved PL (TRPL) decay was tested by an Edinburgh FLS 980 spectrophotometer with 390 nm of excitation wavelength. The electron spin resonance (ESR) signals of the radicals were trapped by 5,5-dimethyl-1-pyrroline *N*-oxide (DMPO) and were detected on a JEOL JES-FA200 spectrometer.

2.3. Photoelectrochemical measurement

The Mott-Schottky curves, electrochemical impedance spectra (EIS) and transient photocurrent responses were evaluated on a Metrohm Autolab PGSTAT204 electrochemical workstation with a standard three-electrode configuration. The electrodes contained a Pt counter electrode, a saturated Ag/AgCl reference electrode and working electrodes, namely UiO-66-NH_2, Bi_5O_7I and BU-5 fabricated on the FTO glasses. In this system, Na_2SO_4 (0.2 mol/L) was applied as electrolyte solution. With respect to the working electrodes, 0.005 g of materials were dispersed in 400 μL ethanol-Nafion (19/1, *v/v*) solution to gain a slurry. After that, the slurry was adhered to the FTO glasses (1 × 1 cm^2) and dried at 60 °C overnight. The light source was based on Perfectlight FX300 high-pressure Xe lamp.

2.4. Photocatalysis experiments on ciprofloxacin degradation

The photocatalytic efficiencies of the as-prepared materials were studied by decomposition of CIP under the illumination of white light. As a light source, a CEL-HXF300 Xe lamp was used (the wavelength distribution spectrum was shown in Electronic Supplementary Information Fig. S1). Before the photocatalytic process, 100.0 mg of photocatalysts were added into the 200.0 mL CIP solution (10.0 mg/L) and the resulting suspension was then stirred for 60 min in dark till adsorption-desorption equilibrium. During the photocatalytic process, about 2.5 mL aliquot was sampled from the solution at pre-set time intervals. To facilitate further analysis and remove the solid matter, the sample was filtrated through a polyethersulfone (PES) membrane of 0.45 μm diameter. The concentration of CIP was detected by a PerkinElmer Lambda 650 S UV–vis spectrophotometer at characteristic wavelength of 276 nm (Lai et al., 2019). The recyclability of the optimal BU-5 photocatalyst was assessed through 4 adsorption-degradation-regeneration runs.

2.5. Identification of the degradation intermediates

The identification of the degradation intermediates was accomplished by a Thermo Dionex UltiMate 3000 ultra-performance liquid chromatography (UPLC) equipped with a Waters Synapt G2-Si quadrupole-time-of-flight mass spectroscopy (Q-TOF-MS) at the positive ion mode. A Acquity BEH C-18 chromatographic column (2.1 mm × 50 mm, 1.7 μm) served to separate the intermediates. The mobile phase was composed by (A) acetonitrile and (B) 0.1% formic acid solution (25/75 *v/v*) at a flow rate of 0.3 mL/min. MS experiments were carried using the instrumental conditions as follows: 2.0 kV capillary voltage, 100 °C temperature of ESI source, 400 °C desolvation temperature, 50.0 L/h cone gas flow, and 800.0 L/h of desolvation gas flow. The MS spectra were recorded over the range of 50–1500 *m/z*.

The generated inorganic products during the photocatalytic process were analyzed by a SHINE CIC-D120 ion chromatography. The SH-AC-3 anion column (250 mm × 4.0 mm) and SH-CC-3 cation column (100 mm × 4.6 mm) were used to analyze the F^- and NH_4^+ ions, respectively, at 35 °C with a flow rate of 1.0 mL/min. For the analysis of F^-, the mobile phase was made up of 2.0 mmol/L Na_2CO_3 and 8.0 mmol/L $NaHCO_3$, while the 5.0 mmol/L solution of methanesulfonic acid was used for NH_4^+ analysis.

2.6. Theoretical calculations

Density functional theory (DFT) based first-principle calculations were performed by the projector-augmented-wave (PAW) method using the Vienna Ab initio Simulation Package (VASP) (Kresse and Furthmüller, 1996a, 1996b). The electronic exchange and related energy were described with the Perdew-Burke-Ernzerhof (PBE) of the generalized gradient approximation (GGA). Weak van der Waals interaction was expected to play a dominant role between UiO-66-NH_2 and Bi_5O_7I. The cutoff energy for electronic wave functions was set as 600 eV. The *k*-point grid integrated in the Brillouin area was geometrically relaxed by 4 × 4 × 1 and sampled by the *k*-grid centered at 4 × 4 × 4 to accurately optimize the structure. Geometry optimizations were terminated when the energy and force on each ion were reduced below 10^{-5} eV and 0.02 eV/Å, respectively. The units of UiO-66-NH_2 were cleaved along (0 0 1) direction to obtain the minimum repetitive unit. The combination of Bi_5O_7I on UiO-66-NH_2 was analyzed on the optimized Bi_5O_7I surface by placing Bi_5O_7I molecular model on the top of UiO-66-NH_2 structure model. An initial vertical distance of 2.5 Å was chosen to allow the interaction between Bi_5O_7I and UiO-66-NH_2.

3. Results and discussion

3.1. Photocatalysts characterization

3.1.1. PXRD and FT-IR spectra

The crystallinity of the Bi_5O_7I, UiO-66-NH_2 and the BU-*x* heterojunctions were firstly characterized by PXRD analysis. As shown in Fig. 2 (a), the as-prepared Bi_5O_7I possessed high crystallinity degree. Meanwhile, all the diffraction peaks can be exactly matched well with the Bi_5O_7I standard card (JCPDS No. 40-0548). Additionally, the as-prepared Bi_5O_7I was indexed to the orthorhombic crystal structure with lattice constants of $a = 16.26$ Å, $b = 5.35$ Å, $c = 11.50$ Å (Chen et al., 2017). Meanwhile, the pristine Bi_5O_7I sample exhibited several

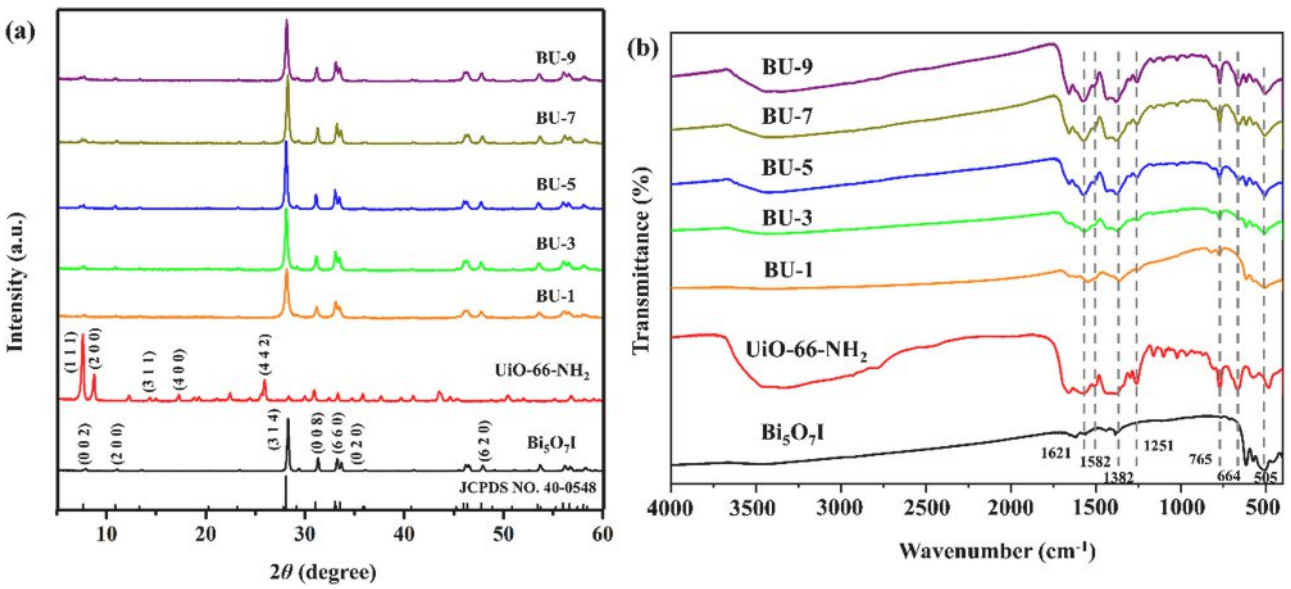

Fig. 2. (a) PXRD and (b) FT-IR spectra of the Bi_5O_7I, UiO-66-NH_2 and BU-*x* heterojunctions.

strong diffraction peaks at $2\theta = 7.7°$, 10.9°, 28.1°, 31.1°, 33.0°, 33.5°, 47.8°, 56.0° and 58.1°, which were assigned to the (0 0 2), (2 0 0), (3 1 4), (0 0 8), (6 6 0), (0 2 0), (6 2 0), (9 1 4) and (6 2 8) planes. The above features suggested the successful fabrication of Bi_5O_7I without any impurities. Furthermore, the pristine UiO-66-NH_2 showed various diffraction peaks, which were in line with the published UiO-66-NH_2 structure (Zhou et al., 2019; Li et al., 2020c), confirming the successful synthesis of UiO-66-NH_2. By comparison, the BU-1 and BU-3 samples exhibited similar PXRD patterns as the pristine Bi_5O_7I without any characteristic peaks of UiO-66-NH_2. This is because of the relatively low amount of UiO-66-NH_2 in the heterojunctions. Similar phenomenon can be observed in our previous reports on MOF/bismuth-based semiconductor composites (Zhao et al., 2020a, 2021b). Anyway, it was no doubt that BU-*x* heterojunctions were successfully constructed via ball-milling treatment for the mixture of Bi_5O_7I and UiO-66-NH_2. With the increase of UiO-66-NH_2, the peak intensities of UiO-66-NH_2 ($2\theta = 7.4°$ and 8.6°) in BU-5, BU-7 and BU-9 increased gradually, suggesting the UiO-66-NH_2 was still able to maintain its crystal texture after the introduction of Bi_5O_7I.

Further characterization of the functional groups of the as-prepared samples was performed by FT-IR. As shown in Fig. 2(b), the absorption spectra of pristine Bi_5O_7I and UiO-66-NH_2 were almost similar to previous reports (Zhou et al., 2019; Li et al., 2020c; Chen et al., 2018b; Geng et al., 2018). More importantly, all the representative peaks of Bi_5O_7I and UiO-66-NH_2 were observed in the different BU-*x* heterojunctions. Additionally, as the amount of UiO-66-NH_2 increased, the corresponding intensities of absorption peaks were inclined to reinforce. Among all the characteristic peaks in BU-*x*, the strong peaks at 1621 cm^{-1} and 1582 cm^{-1} were indexed to the benzene ring and C═O stretching (Xu et al., 2018; Yang et al., 2019). The C═C and C—C vibration mode of the organic ligand in MOFs appeared at 1500–1400 cm^{-1} (Lin et al., 2015; Zhu et al., 2014). The peaks located at 1382 cm^{-1} and 1251 cm^{-1} in BU-*x* heterojunctions were attributed to the stretching vibration of the C—N bond (Kardanpour et al., 2015), the peaks at 765 cm^{-1} and 664 cm^{-1} belonged to O—H and C—H vibration in the NH_2-BDC ligand (Hu et al., 2019), while the absorption band at 800–600 cm^{-1} was attributed to the Zr—O in UiO-66-NH_2 (Yang et al., 2019). It was worth noting that all the BU-*x* samples displayed a characteristic peak at 505 cm^{-1}, which was associated with the stretching vibration of Bi–O bond from Bi_5O_7I (Liu, 2015; Liu et al., 2015). According to PXRD and FT-IR results, it seems certain that BU-*x* heterojunctions were successfully fabricated via ball-milling method.

3.1.2. Morphology analysis

To examine the morphology and micro-structure of the as-prepared materials, SEM, TEM and HRTEM analysis were performed. Fig. 3(a) and (d) exhibited the SEM and TEM images of UiO-66-NH_2. As-synthesized UiO-66-NH_2 exhibited a smooth octahedral morphology with diameters of 250–500 nm, which was consistent with the previous studies (Zhou et al., 2019; Li et al., 2020c; Yang et al., 2019). As to pristine Bi_5O_7I, it displayed a three-dimensional coral-like structure constructed by the self-assembled agglomerated nanorods with uneven sizes of 500 nm–2 μm in length (Fig. 3(b) and (e)). In this section, BU-5 was selected as the representative sample of BU-*x* heterojunctions for morphology analysis. As shown in Fig. 3(c) and (f), the BU-5 basically kept the regular octahedral structure after ball-milling process. However, the coral-like morphology of Bi_5O_7I completely disappeared and transformed into a plenty of nanorods with diameters of 50–100 nm. Furthermore, it was clearly observed that relatively small Bi_5O_7I nanorods tightly adhered on the surface of UiO-66-NH_2 octahedrons, resulting in increasement of the surface roughness. More importantly, the TEM and HRTEM images of BU-5 (Fig. 3(f)–(h)) exhibited closed interaction between Bi_5O_7I and UiO-66-NH_2, which was expected to stimulate the transfer of photo-generated hole-electron pairs, thus leading to boost the apparent photocatalytic reaction rate. The corresponding HRTEM image (Fig. 3(h)) exhibited the lattice fringes of 0.31 nm, 0.28 nm and 0.19 nm, which were assigned to the (1 1 6), (4 0 6) and (2 1 11) planes of Bi_5O_7I. Meanwhile, the series of concentric rings in the SAED (Fig. 3(i)) were indexed to the (2 0 2), (2 0 12), (0 0 2) and (1 3 4) planes of Bi_5O_7I (JCPDS No. 40-0548). To further identify the successful formation of Bi_5O_7I/UiO-66-NH_2 heterojunctions, the elemental mapping analysis was also carried out for any selected region in the SEM image of BU-5. As shown in Fig. S2, it can be found that Zr, Bi, I, O, and N elements were uniformly distributed on the surface of UiO-66-NH_2 octahedron, suggesting that the successful loading of the Bi_5O_7I nanorods on the surface of octahedron UiO-66-NH_2, which matched well with the SEM, TEM and HRTEM results.

3.1.3. Optical and surface area analysis

The optical absorption property of a photocatalyst play significant role in photocatalytic activity. UV–vis DRS spectra of UiO-66-NH_2, Bi_5O_7I and BU-*x* heterojunctions were illustrated in Fig. 4(a). The pristine Bi_5O_7I exhibited an absorption edge at approximately 415 nm, suggesting that Bi_5O_7I can undergo excitation by UV light and a fraction of visible light. In contrast, the as-prepared UiO-66-NH_2 displayed a

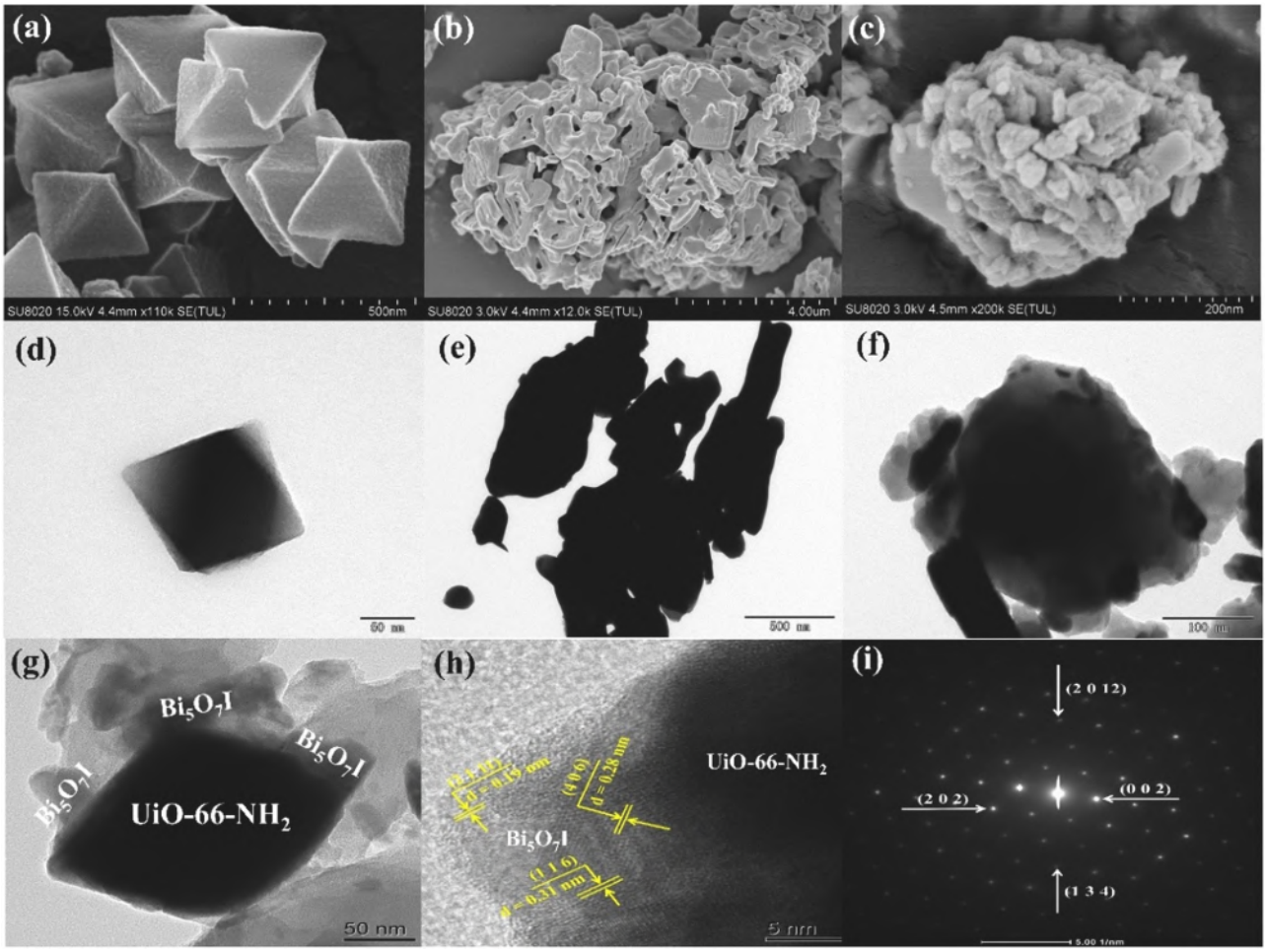

Fig. 3. SEM and TEM images of (a, d) UiO-66-NH_2, (b, e) Bi_5O_7I, (c, f) BU-5 and (g-h) HRTEM images and (i) SAED image of BU-5.

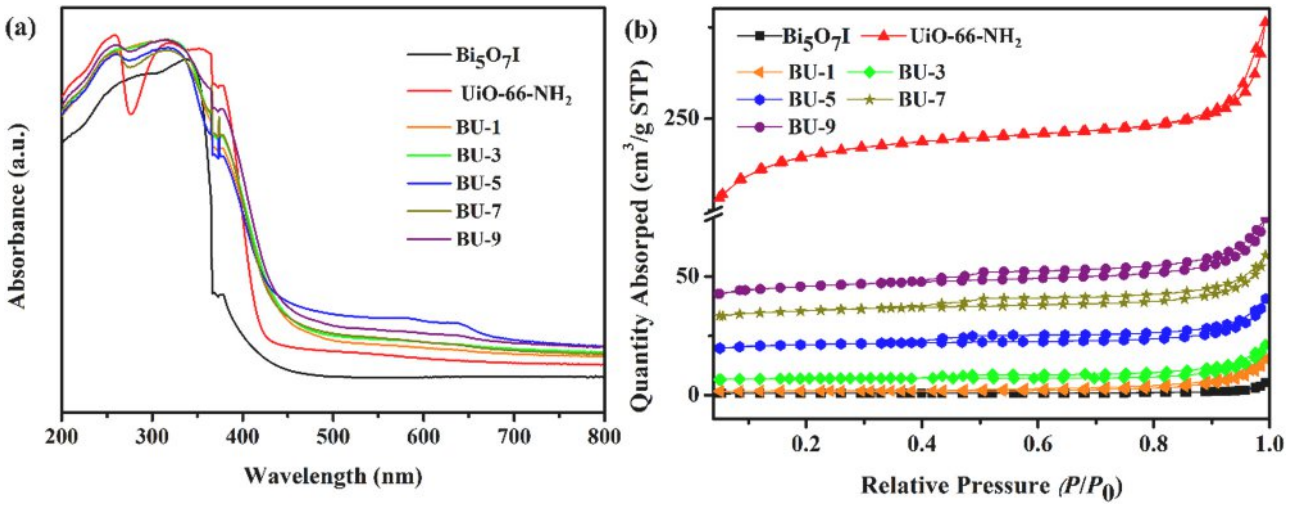

Fig. 4. (a) UV–vis DRS spectra and (b) N_2 adsorption-desorption isotherms of Bi_5O_7I, UiO-66-NH_2 and BU-*x* heterojunctions. (For interpretation of the references to colour in this figure legend, the reader is referred to the web version of this article.)

longer absorption edge of 421 nm, which can absorb more visible light energy. With respect to BU-*x* samples, their absorption edges were red-shifted compared with the pristine Bi_5O_7I and UiO-66-NH_2. Moreover, the photo-responsive capacities in visible light region of BU-*x* were orderly enhanced by increasing the amount of UiO-66-NH_2 in the heterojunctions, indicating the introduction of UiO-66-NH_2 was beneficial to reinforce the photo-exciting process during photocatalytic reaction. The following Eq. (1) was used to calculate the bandgap energies of the as-prepared samples:

$$\alpha h\nu = A(h\nu - E_g)^n \quad (1)$$

where h is the Planck's constant, α represents absorption coefficient, ν is the frequency of light, E_g is the bandgap. The value of n is related to the optical transition of the semiconductors. For UiO-66-NH_2, the n value was 1 for direct transition (Mu et al., 2018), whereas the n value of Bi_5O_7I was 4 for indirect transition (Liu et al., 2015; Cheng et al., 2019). As shown in Fig. S3(a)-(b), the bandgaps of Bi_5O_7I and UiO-66-NH_2 were determined as 2.98 eV and 2.94 eV, which were in good accordance with previous reports (Xu et al., 2020; Zhou et al., 2019; Li et al., 2020c). The bandgaps of BU-1, BU-3, BU-5, BU-7 and BU-9 were 2.90 eV, 2.87 eV, 2.85 eV, 2.83 eV and 2.80 eV, respectively. The above results suggested that BU-x heterojunctions can be excited by white light.

The photocatalytic activity of a photocatalyst is strongly bound up with the corresponding specific surface area. The N_2 adsorption-desorption isotherms and pore size distribution curves of Bi_5O_7I, UiO-66-NH_2 and BU-x were shown in Figs. 4(b) and S4(a)–(g). It was obvious that UiO-66-NH_2 rapidly absorbed a large amount N_2 at relatively low pressures due to it is a microporous material. By contrast, the adsorption isotherm of Bi_5O_7I belonged to Type II with a feature of macroporous structure. With respect to BU-x samples, all the isotherms were assigned to typical Type IV with hysteresis loops of H3 and high relative pressure of 0.4–1.0. According to IUPAC classification, this trait should be attributed to the typical mesoporous structure, which might originate from the aggregations of the Bi_5O_7I nanorods and co-existence of UiO-66-NH_2 (Yin et al., 2020; Santhoshkumar et al., 2019). The total pore volume, BET surface area, and average pore size of the prepared materials are provided in Table 1. Obviously, with the increase of UiO-66-NH_2 content in the heterojunctions, the pore volume and specific surface area of the BU-x samples gradually increased, even though they exhibited moderate decrease as compared to pristine UiO-66-NH_2. It is well known that large surface area provided sufficient adsorption and reaction sites for pollutants, thus finally enhancing the photocatalytic efficiency (Wang et al., 2019b, 2020). Therefore, it can be forecasted that BU-x heterojunctions might display improved photocatalytic activity for organic contaminant removal.

3.1.4. XPS analysis

The elemental compositions and surface chemical states of BU-5 were analyzed by XPS. As presented in Fig. 5(a), the signals of C, N, O, Bi, Zr and I were detected in the XPS survey spectrum of the as-prepared BU-5, which agreed well with the PXRD and EDS mapping results. The high-resolution C 1s spectrum (Fig. 5(b)) could be divided into three peaks located at 288.8 eV (O—C═O), 286.3 eV (C—O) and 284.8 eV (C—C) groups of NH_2-BDC (Zhou et al., 2019). For the spectrum of O 1s (Fig. 5(c)), two characteristic peaks at 531.6 eV and 530.2 eV may be attributed to –OH, Bi–O and Zr–O bonds of BU-5, respectively (Hu et al., 2019; Mei et al., 2019; Mi et al., 2014; Zhu et al., 2018). Fig. 5(d) showed that the N 1s spectrum can be curve-fitted into two peaks at 400.2 eV and 398.9 eV, which were relevant to –NH– and –NH_2 groups of organic ligand in UiO-66-NH_2 (Zhou et al., 2019; Iqbal et al., 2008; Zhang et al., 2013). As depicted in Zr 3d spectrum (Fig. 5(e)), the peaks at 185.2 eV and 182.8 eV represented the Zr $3d_{3/2}$ and Zr $3d_{5/2}$ of UiO-66-NH_2 in BU-5 sample (Ding et al., 2017). Moreover, the high-resolution spectrum of I 3d exhibited two strong peaks at 631.1 eV and 619.7 eV (Fig. 5(f)), which can be indexed to I $3d_{3/2}$ and I $3d_{5/2}$ and revealed that the valence of I in the BU-5 was − 1 (Li et al., 2020a; Zeng et al., 2016). Meanwhile, the Bi $4f_{5/2}$ and Bi $4f_{7/2}$ peaks of BU-5 were located around 164.4 eV and 159.1 eV, respectively (Fig. 5(g)), indicating the valence of Bi in the BU-5 was + 3 (Liang et al., 2019). Therefore, the valence states of Bi and I suggested that the existence of Bi_5O_7I in the BU-5 sample. More importantly, the binding energies of I 3d and Bi 4f in BU-5 were higher than those of Bi_5O_7I, while the binding energies of Zr 3d were lower than those of UiO-66-NH_2. This should be ascribed to the increased electron density on Zr atoms and the decreased electron densities on Bi and I atoms in the BU-5 heterojunction. Therefore, the XPS results confirmed the electron donation and strong chemical interaction between Bi_5O_7I and UiO-66-NH_2, which was consistent with the SEM, TEM and HRTEM analysis. Additionally, ICP-OES and XPS were used to determine the molar ratios of Bi/Zr. As shown in Table S1, the ratios determined by XPS were larger than those determined by ICP-OES. In other words, the surface content of Bi_5O_7I was larger than the bulk one, which might be beneficial to enhance the photocatalytic activities of the as-prepared BU-x samples under white light irradiation.

Table 1
BET surface area, average pore size and total pore volume of the as-prepared samples.

Samples	S_{BET} (m^2/g)	Average pore size (nm)	Total pore volume (cm^3/g)
Bi_5O_7I	2.29	15.703	0.007
UiO-66-NH_2	729.02	2.318	0.422
BU-1	5.53	12.448	0.022
BU-3	21.65	5.625	0.030
BU-5	66.03	3.615	0.059
BU-7	109.89	3.203	0.088
BU-9	141.83	3.151	0.112

3.2. Photocatalytic degradation of ciprofloxacin

The photocatalytic performances of Bi_5O_7I, UiO-66-NH_2 and BU-x materials were explored by CIP degradation under white light illumination. Experiments were conducted to check the activities of various photocatalysts for 10.0 mg/L of CIP with sample dosage of 0.5 g/L, normal solution pH being 5.8 and illumination time of 120 min in the reactor. As illustrated in Fig. 6(a), no remarkable CIP decomposition was found by direct photolysis under the illumination of white light, only 25.7% of CIP was photodegraded within 180 min. As the used white light was a broad spectrum of different wavelengths containing ultraviolet A (UVA) and visible light sources (Fig. S1), earlier studies had proved that the fluoroquinolones could absorb light in the UVA region to produce some reactive oxygen species (ROS) like $^1O_2$, $\cdot O_2^-$ and ·OH (Agrawal et al., 2007; Sarkhosh et al., 2019), which may contribute to CIP removal. However, this result revealed that direct photolysis alone could not be applied as impressive procedure for CIP removal from aqueous solutions. Before photocatalytic degradation, the as-prepared materials adsorbed CIP for 60 min in darkness condition to achieve adsorption-desorption equilibrium. It was observed that only 1.9% of CIP was adsorbed by Bi_5O_7I, while 13.4% of CIP was adsorbed by UiO-66-NH_2. Considering that the BET surface area and total pore volume of UiO-66-NH_2 were 729.02 m^2/g and 0.422 cm^3/g, respectively, which were much larger than that of Bi_5O_7I (0.98 m^2/g and 0.003 cm^3/g). Hence the main reason for this phenomenon was due to different pore volumes and specific surface areas of the samples, more adsorption reactive sites and pollutant transport channels can be provided by UiO-66-NH_2, thus enhancing the corresponding CIP adsorption capacity. It was worth noting that the adsorption capacities of BU-x samples were between Bi_5O_7I and UiO-66-NH_2, the addition of UiO-66-NH_2 significantly improved the CIP adsorption potential of BU-x, and BU-9 possessed a maximum adsorption efficiency of 11.5%. The next 120 min included the process of photocatalytic degradation. Obviously, the CIP photocatalytic degradation by pristine Bi_5O_7I and UiO-66-NH_2 were inefficient, only 46.0% and 37.4% of CIP were decomposed under white light irradiation. However, it can be seen that BU-x heterojunctions exhibited prominently higher ability in degradation of CIP compared with pristine Bi_5O_7I and UiO-66-NH_2. With the increasing weight percentage of UiO-66-NH_2 from 10% to 90%, the photocatalytic efficiency was gradually enhanced and then decreased owing to superfluous UiO-66-NH_2 may block the active sites presented on the Bi_5O_7I surface. The highest degradation percentage of 82.2% was achieved by the BU-5 after 180 min of adsorption-degradation process. More importantly, under identical conditions, degradation efficiency of

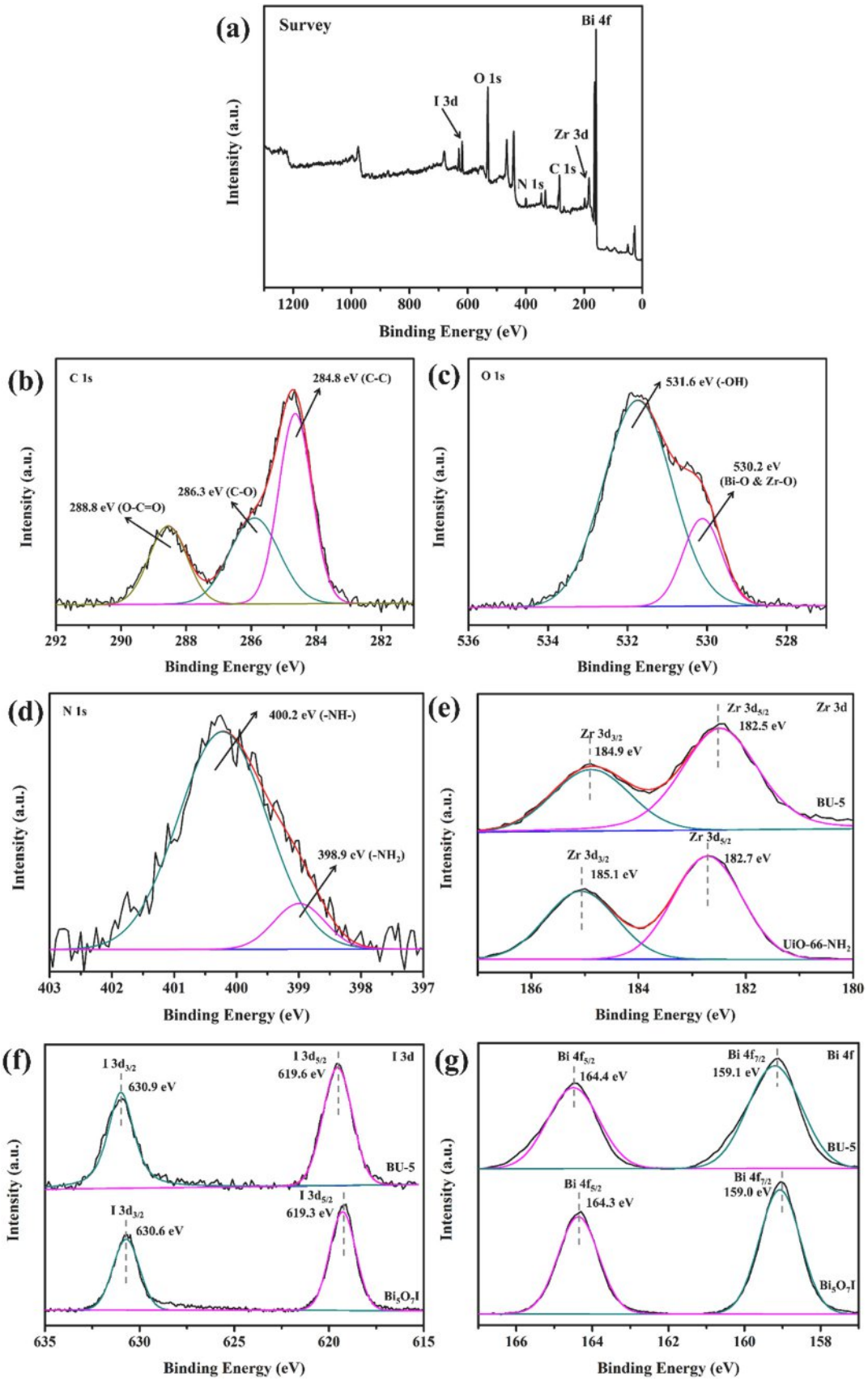

Fig. 5. (a)–(f) Survey, C 1s, O 1s, and N 1s high-resolution XPS spectra of the BU-5 heterojunction, (g) the comparison of Zr 3d, I 3d and Bi 4f spectra between BU-5 and Bi_5O_7I.

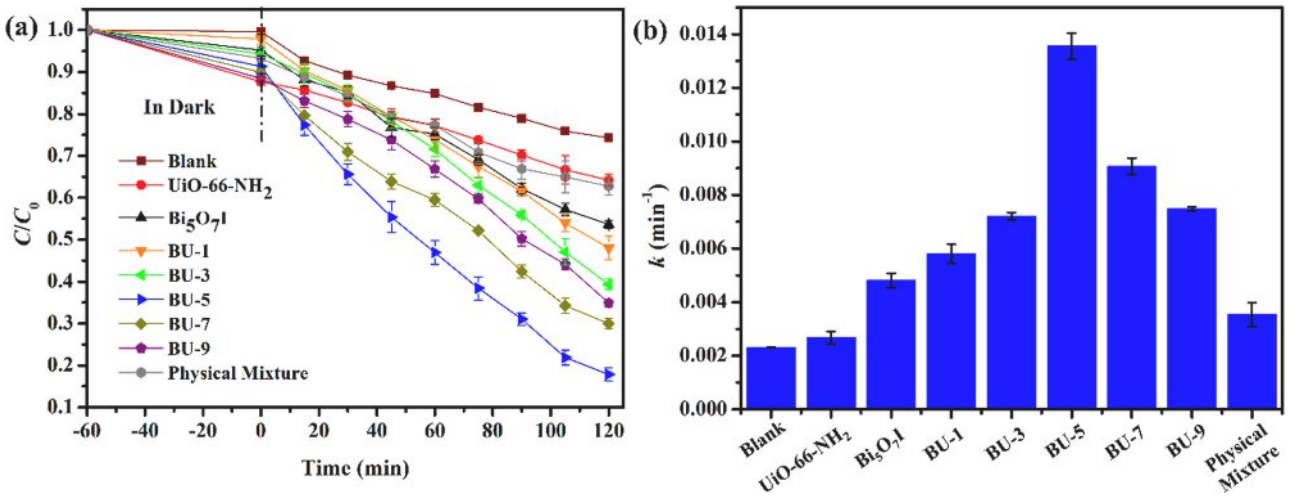

Fig. 6. (a) Photocatalytic degradation of CIP using various photocatalysts irradiated with white light and (b) their corresponding k values, condition: CIP = 10 mg/L, sample dosage = 0.5 g/L, pH = 5.8.

CIP solution over the physical mixture of Bi_5O_7I and UiO-66-NH_2 were only 37.2% after 120 min of illumination time. Thus, the synergistic effect can be achieved by the combination of Bi_5O_7I and UiO-66-NH_2 via ball-milling process, which may be ascribed to the formation of BU-x heterojunctions can enhance light absorption efficiency, accelerate the transfer rate of photo-generated electron-hole pairs and reinforce the oxidation ability for organic pollutants. Meanwhile, reaction kinetics for CIP degradation was determined through pseudo-first-order reaction kinetic model by using Eq. (2) (Liu et al., 2019; Yu et al., 2019):

$$-\ln(C_t/C_0) = kt \quad (2)$$

where C_t denotes the CIP concentration at time t while C_0 represent time zero, k is the degradation rate constants. As depicted in Fig. 6(b), the order of k value was observed as UiO-66-NH_2 (0.0026 ± 0.000156 min^{-1}) < physical mixture (0.00353 ± 0.000438 min^{-1}) < Bi_5O_7I (0.00497 ± 0.000106 min^{-1}) < BU-1 (0.0058 ± 0.00 0354 min^{-1}) < BU-3 (0.00721 ± 0.000141 min^{-1}) < BU-9 ($0.00749 \pm$ 0.000078 min^{-1}) < BU-7 (0.00907 ± 0.000311 min^{-1}) < BU-5 (0.01 356 ± 0.000488 min^{-1}). Apparently, the optimal BU-5 displayed the highest k value, which was 5.22 and 2.73 times higher compared with pristine UiO-66-NH_2 and Bi_5O_7I, respectively. All the above results demonstrated that BU-x heterojunctions could effectually improve the CIP photodegradation activity under white light irradiation.

3.2.1. *Effect of photocatalyst dosages*

As to photocatalytic process, the photocatalyst dosage in reaction system will directly influence the corresponding number of active sites and yield of free radicals. Therefore, effect of varying BU-5 dosages (0.25, 0.50, 0.75 and 1.00 g/L) on photodegradation of CIP was evaluated at constant concentration of CIP (10 mg/L) and pH value of 5.8 (natural condition). As illustrated in Fig. 7(a), with the increased dosage of BU-5 from 0.25 g/L to 1.00 g/L, the adsorption capacities toward CIP in darkness gradually rose from 6.2% to 34.7% owing to the enhancive number of available adsorption sites of BU-5 particles. More importantly, the total removal efficiencies and apparent reaction rates of CIP were accordingly increased with an optimal dosage of 0.75 g/L (total removal efficiency reached to 96.1%), which should be ascribed to more active free radicals might be generated by larger amounts of the photocatalyst. However, the maximum dosage used in this study (1.00 g/L) resulted in a slightly decreased total removal efficiency and apparent reaction rate. According to Fig. 7(b), the k values followed the order of 0.25 g/L (0.01103 ± 0.000127 min^{-1}) < 0.50 g/L (0.01356 ± 0.00 0488 min^{-1}) < 1.00 g/L (0.01415 ± 0.000622 min^{-1}) < 0.75 g/L (0.02694 ± 0.000643 min^{-1}). The decrease at the high BU-5 dosage was probably ascribed to light scattering resulting from the increased turbidity and the subsequent reduction in the white light penetration and the photocatalytic reaction rate (Vaiano et al., 2018; Zhao et al., 2018). The measured turbidities for the BU-5 dosage increasing from

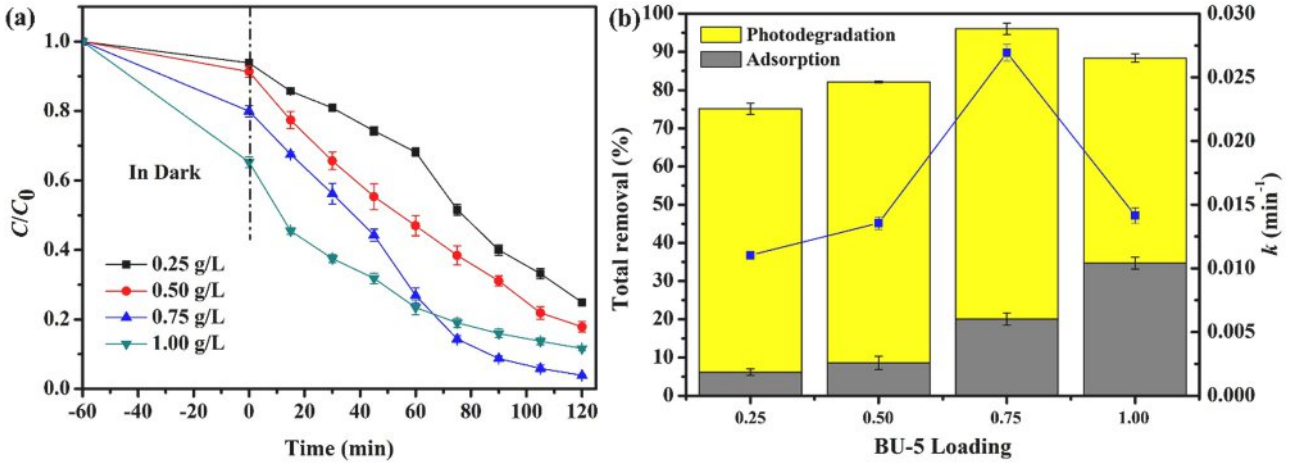

Fig. 7. (a) Adsorption-photocatalytic curves of CIP under different BU-5 loadings and (b) the corresponding degree of adsorption, photodegradation and k values, condition: CIP = 10 mg/L, pH = 5.8.

0.25 g/L to 1.00 g/L were 360 NTU, 640 NTU, 1092 NTU and 1588 NTU, respectively. Since no enhanced removal of CIP could be observed above the 0.75 g/L dosage of BU-5, thus the optimal dosage of BU-5 was set as 0.75 g/L. Meanwhile, being compared with the reported photocatalysts, the BU-5 in this study did possess a competitive performance towards CIP removal (Table 2).

3.2.2. Effect of initial pH

The pH of the solution is one of the crucial environmental factors that can dramatically influence the photocatalytic process. However, the interpretation of pH effect on the photocatalytic process is a tough task since it determines the surface electrical properties of photocatalyst, existing forms of target organic pollutant and formation mechanism of active free radicals in the reaction system (Wang et al., 2019b, 2016, 2020; Zhao et al., 2021a). In the current research, the influence of initial pH on the adsorption-photodegradation of CIP in aqueous suspensions of BU-5 was investigated at pH values being 3.0, 5.8, 7.0 and 9.0. The dosage of BU-5 and CIP concentration were set as 0.75 g/L and 10 mg/L, respectively. As expected, the solution pH possessed a remarkable effect on the capacity to adsorb the CIP molecules (Fig. 8(a)). The adsorption capacities of CIP were only 12.6% and 8.7% at pH = 3.0 and 9.0, whereas the adsorption capacities increased to 20.1% and 24.6% at pH = 5.8 and 7.0, respectively. This phenomenon can be attributed to the point of zero charge (pH_{PZC}) of BU-5 and the charge characteristic of CIP molecules. Fig. S5 displayed the Zeta potentials of BU-5 under different pH values. The pH_{PZC} of BU-5 was calculated to be 3.74, indicating that the BU-5 surface will remain positively charged at pH < 3.74 and negatively charged at pH > 3.74. Furthermore, the CIP exhibited zwitterionic characteristic with two pK_a values of 6.2 and 8.8 (Dodd et al., 2005). Therefore, under the acid condition (pH < pK_{a1} = 6.2), CIP possesses a positive charge on its piperazinyl group, whereas CIP exists as a negative charge on its carboxylic moiety under the alkaline condition (pH > pK_{a2} = 8.8). At neutral pH both cationic and anionic species are in dynamic equilibrium, thus CIP could reach the equipotential point (Dodd et al., 2005; Gad-Allah et al., 2011). Based on the above results, it should be inferred that there were strong electrostatic repulsion between CIP and the BU-5 at pH = 3.0 and 9.0, leading to the low adsorption capacities toward CIP molecules. In general, the pre-adsorption behavior for the target pollutant will inevitably affect the subsequent photocatalytic activity. Fig. 8(b) showed that the photodegradation rate increased to a peak at pH = 7.0 and started to decrease with further increasing solution pH, following was the order of corresponding k values at pH = 7.0 ($0.03402 \pm 0.000628\ min^{-1}$) > pH = 5.8 ($0.02694 \pm 0.000643\ min^{-1}$) > pH= 9.0 ($0.01522 \pm 0.000177\ min^{-1}$) > pH = 3.0 ($0.01133 \pm 0.000834\ min^{-1}$). The high photocatalytic rate in case of pH = 7.0 can be attributed to two reasons as follows. Firstly, neutral condition was beneficial to ·OH production via h^+ oxidation of H_2O or OH^-, thus enhancing the efficiency of ·OH attack on CIP molecules (Zhao et al., 2018a). Secondly, when the solution pH was close to the equipotential point of CIP (approximately 7.5) (Dodd et al., 2005), the CIP will absorb photons to form its photoexcited state with poor stability, which was inclined to be decomposed more rapidly (Guo et al., 2013; Dodd et al., 2005).

3.2.3. Effect of inorganic anions

The photodegradation efficiency of organic pollutant significantly affected by the presence of co-existing anions, since the anions serve as a function of free radical scavengers and involve in the generation of weaker anion reactive species (Wang et al., 2018). The influence of anions on the photodegradation of CIP was estimated by adding 1.0 mM of Cl^-, SO_4^{2-}, $H_2PO_4^-$ and NO_3^- to the CIP solutions. The effect of each anion is provided in Fig. 9(a) and the maximum inhibition on CIP removal was observed by the $H_2PO_4^-$, the corresponding removal efficiency decreased to 75.9%. In contrast, the presence of Cl^- possessed inappreciable influence on the CIP photodegradation, the ultimate removal efficiency also reached to 96.0%. Moreover, as shown in Fig. 9 (b), the inhibition effects of different anions calculated by k values followed the order of without co-existing anions ($0.02694 \pm 0.000643\ min^{-1}$) > Cl^- ($0.02320 \pm 0.000544\ min^{-1}$) > NO_3^- ($0.01479 \pm 0.000884\ min^{-1}$) > SO_4^{2-} ($0.01253 \pm 0.000417\ min^{-1}$) > $H_2PO_4^-$ ($0.01080 \pm 0.000332\ min^{-1}$). As to $H_2PO_4^-$, the reduction in CIP degradation rate was related to the consumption or reaction with reactive species like ·OH and h^+ based on Eqs. (3) and (4). The generated H_2PO_4· is weaker oxidizing agent than ·OH (Zhao et al., 2021b, 2018), thus affecting the photocatalytic activity of BU-5. The lower CIP photodegradation activity with addition of SO_4^{2-} may be associated with the quenching effect of SO_4^{2-} on ·OH and the production of SO_4^-· via electron transfer process (Eq. (5)) (Chen et al., 2018a). SO_4^-· radical displays a bigger molecular structure with high selectivity as compare to ·OH radical, thereby providing less chance to interact with organic pollutants (Wang and Chu, 2012). Liu and the co-workers (Liu et al., 2016) suggested that in the ·OH dominating process, NO_3^- possessed negligible inhibitory effect on the degradation of organic pollutants. Differently, a moderate reduction of CIP removal efficiency (85.2%) can be found after 120 min of white light illumination. It is associated with the N atom present in piperazinyl structure of CIP molecule was inclined to be oxidized to NO_3^- via attack of ·OH radicals, as expressed in Eq. (6) (Chen et al., 2018a). In view of Le Chatelier's principle, the yield of NO_3^- might reduce the CIP degradation rate. Interestingly, the Cl^- induced the lowest inhibitory effect on the CIP photodegradation process. As seen from Eqs. (7) and (8), the Cl^- can be transformed into $HOCl^-$· upon reaction with ·OH, which can subsequently form Cl· radical (Liao et al., 2001). Considering the secondary oxidizing agents of $HOCl^-$· and Cl· were both significantly effective towards the degradation of organic pollutants and basically keep the same level as ·OH (Chen et al., 2018a; Saleh et al., 2019), thus the reaction rate was slightly decreased.

$$H_2PO_4^- + \cdot OH \rightarrow H_2PO_4\cdot + OH^- \quad (3)$$

$$H_2PO_4^- + h^+ \rightarrow H_2PO_4\cdot \quad (4)$$

$$SO_4^{2-} + \cdot OH \rightarrow SO_4^-\cdot + H_2O \quad (5)$$

Table 2
Comparison of the CIP removal efficiencies achieved by the reported photocatalysts.

Photocatalyst	CIP concentration (mg/L)	Irradiation time (min)	Dosage (g/L)	Efficiency (%)	Light source	Reference
$Bi_4O_5Br_2$	10	120	0.50	75.0	300 W Xe lamp (> 400 nm)	(Di et al., 2015)
$CuS/BiVO_4$	10	90	1.00	86.7	300 W Xe lamp (> 400 nm)	(Lai et al., 2019)
$CNT/PbBiO_2Br$	10	150	0.30	88.0	300 W Xe lamp (> 400 nm)	(Wang et al., 2019a)
$CQDs/PbBiO_2Cl$	10	75	0.30	79.0	300 W Xe lamp (> 400 nm)	(Sheng et al., 2019)
BiOI/MIL-88B(Fe)	10	270	0.30	~80.0	150 W Xe lamp (> 425 nm)	(Jahurul Islam et al., 2017)
Pt/N-BiOCl	10	150	0.20	82.0	300 W Xe lamp	(Maimaitizi et al., 2020)
$BiOBr/Bi_2MoO_6$	10	120	0.20	85.0	300 W Xe lamp (> 420 nm)	(Wang et al., 2017)
$BiOCl/Bi_2WO_6$	10	300	1.00	65.0	300 W Xe lamp (> 420 nm)	(Ma et al., 2016)
$g\text{-}C_3N_4/rGO/WO_3$	20	180	0.20	85.0	500 W Xe lamp (> 400 nm)	(Lu et al., 2019)
CeO_2-Ag/AgBr	10	120	1.00	93.1	300 W Xe lamp (> 420 nm)	(Wen et al., 2018)
BU-5	10	120	0.75	96.1	300 W Xe lamp	This work

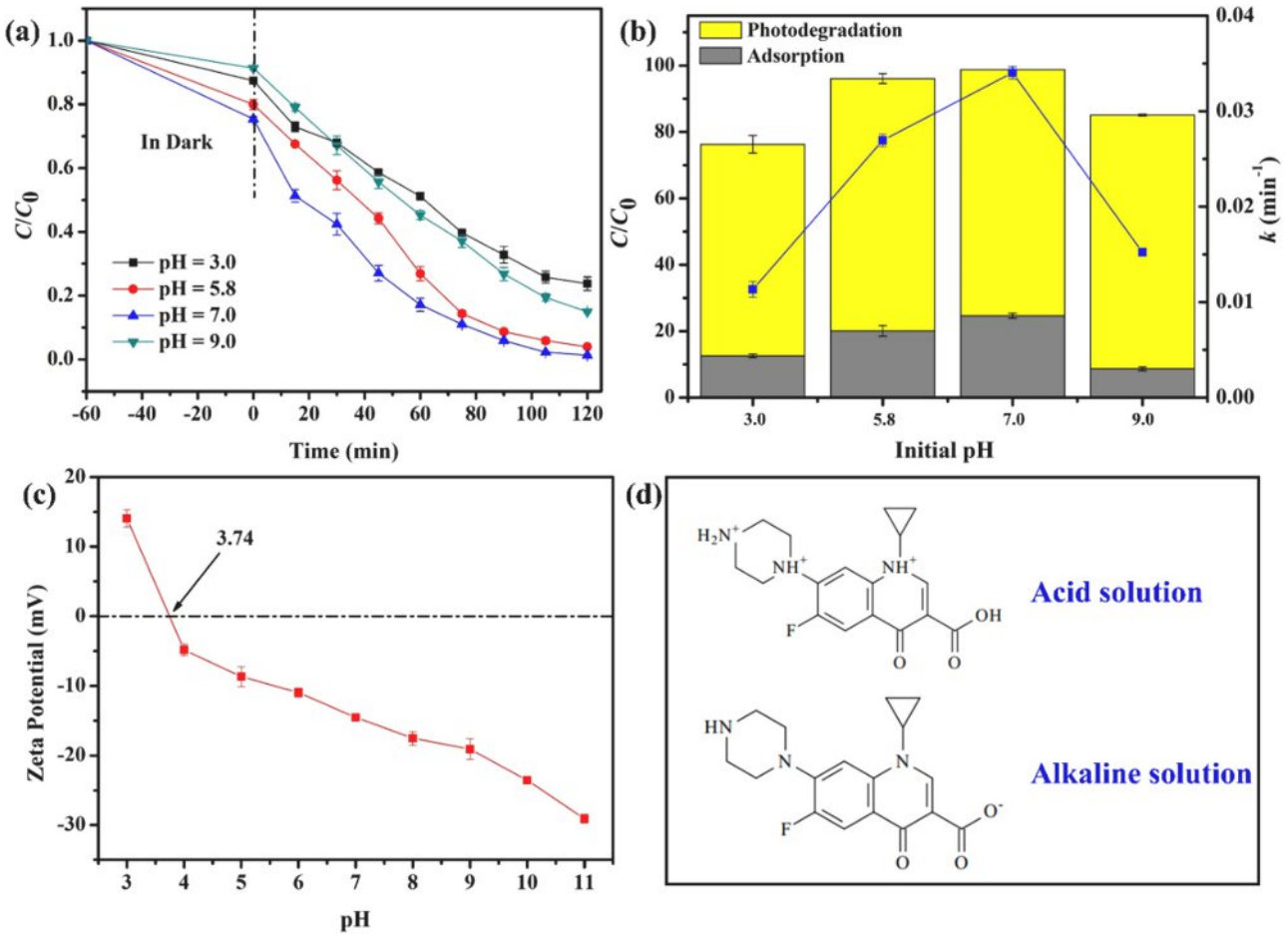

Fig. 8. (a) Effects of different initial pH values on CIP adsorption-photocatalytic degradation process, (b) the corresponding degree of adsorption, photodegradation and k values, condition: CIP = 10 mg/L, BU-5 = 0.75 g/L.

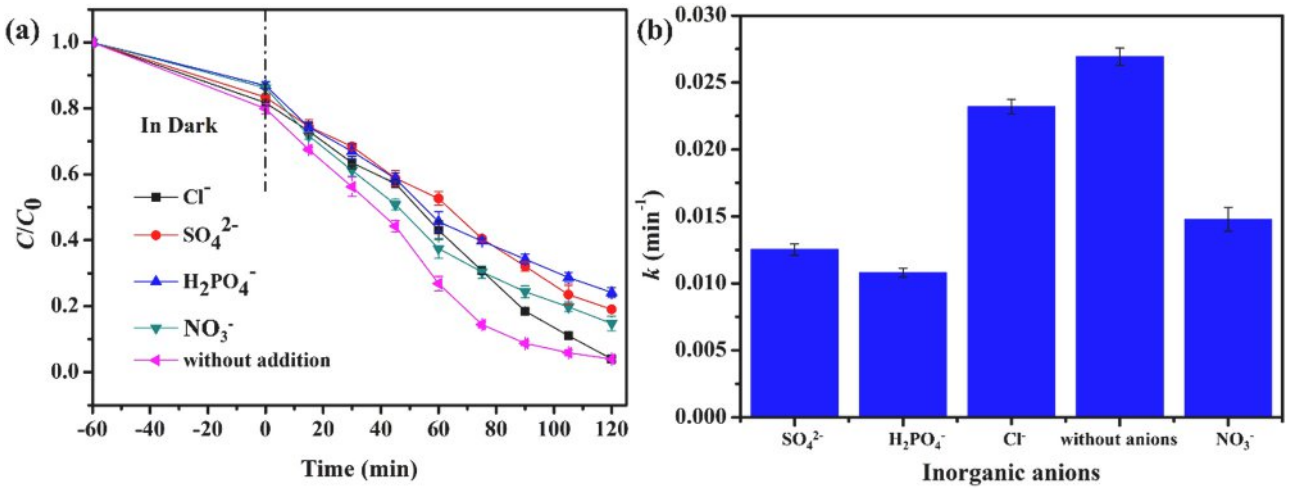

Fig. 9. (a) Effect of inorganic anions on the CIP degradation over the BU-5 and (b) the corresponding k values, condition: BU-5 = 0.75 g/L, CIP = 10 mg/L, pH = 5.8, anions = 1.0 mM.

$$CIP\text{-}N + \cdot OH \rightarrow NO_3^- \quad (6)$$

$$Cl^- + \cdot OH \rightarrow HOCl^- \cdot \quad (7)$$

$$HOCl^- \cdot + H^+ \rightarrow Cl \cdot + H_2O \quad (8)$$

3.3. Reusability and stability of UiO-66-NH_2/Bi_5O_7I heterojunction

To examine the potential practice of the Bi_5O_7I/UiO-66-NH_2 heterojunctions, the reusability and stability of the representative BU-5 had

also been investigated. As illustrated in Fig. 10(a), no distinct decline was observed in photocatalytic efficiency of BU-5 in the removal of CIP after four consecutive runs, the corresponding adsorption-photodegradation efficiency still maintained at 90.4%. Meanwhile, to further explore the photocatalytic stability, the PXRD, FT-IR patterns and XPS survey spectra of BU-5 before and after reaction were examined. As shown in Fig. 10(b)–(d), its crystallinity, functional groups and elemental compositions were almost unchanged throughout 4 cycles. Additionally, TEM image (Fig. S6) revealed no morphology changes in BU-5 after 720 min of adsorption-photocatalytic operation. According to the above results, it should be suggested that the as-prepared BU-5 possessed preferable stability during the photocatalytic process.

3.4. Mechanism of enhanced photocatalysis

Commonly, the separation and transfer efficacy of photo-generated carriers significantly influence photocatalytic efficiency. On this account, the photoelectric performances of as-prepared Bi_5O_7I, UiO-66-NH_2 and BU-5 samples were investigated by steady/time-resolved PL, photocurrent density and EIS techniques. As depicted in Fig. 11(a), the BU-5 owned the lower PL intensity than pristine Bi_5O_7I and UiO-66-NH_2, suggesting that better separative performance was obtained by this sample and the formation of heterojunction between UiO-66-NH_2 and Bi_5O_7I accelerated the migration of photo-generated electron-hole pairs (Zhao et al., 2020a, 2021b; Yi et al., 2019). Afterwards, the EIS was introduced to examine the kinetic of charge transfer at the interface of various heterojunction components. The EIS Nyquist plots (Fig. 11(b)) illustrated that the BU-5 displayed a smaller arc radius compared with pristine Bi_5O_7I and UiO-66-NH_2, revealing that it possessed a lower charge transfer resistance (R_{ct}) and the first-class charge transfer ability (Li et al., 2020c; Chen et al., 2020). Meanwhile, being compared with pristine Bi_5O_7I and UiO-66-NH_2, an apparent improvement in photocurrent response density was exhibited by the BU-5 sample (Fig. 11(c)). Generally speaking, the separative ability of charge carrier is in positive correlation with the photocurrent density (Zhao et al., 2020a, 2021b; Yi et al., 2019; Chen et al., 2020). The more charge carriers remain in the photocatalytic system, the better conductivity can be achieved. Therefore, this result supported the conclusion obtained from steady-state PL spectra and EIS Nyquist plots. Furthermore, time-resolved PL spectra were applied to assess the quantum lifetime of charge carriers. As illustrated in Fig. 11(d), the average life-time ($\tau_{average}$) of BU-5 (1.21 ns) exhibited decent improvement over those of UiO-66-NH_2 (0.66 ns) and Bi_5O_7I (1.03 ns). This can be attributed to photo-generated electrons were inclined to transform between different materials to enhance the spatial separation of electron-hole pairs, thus prolonging the quantum lifetime of BU-5 photocatalyst (Zhao et al., 2020a; Yi et al., 2020). This transformation may provide more possibilities of photo-generated electrons to be involved in the photocatalytic reaction, thus ultimately leading to the greatest CIP photodegradation efficiency. For purpose of understanding the mechanism of photo-generated carriers migration,

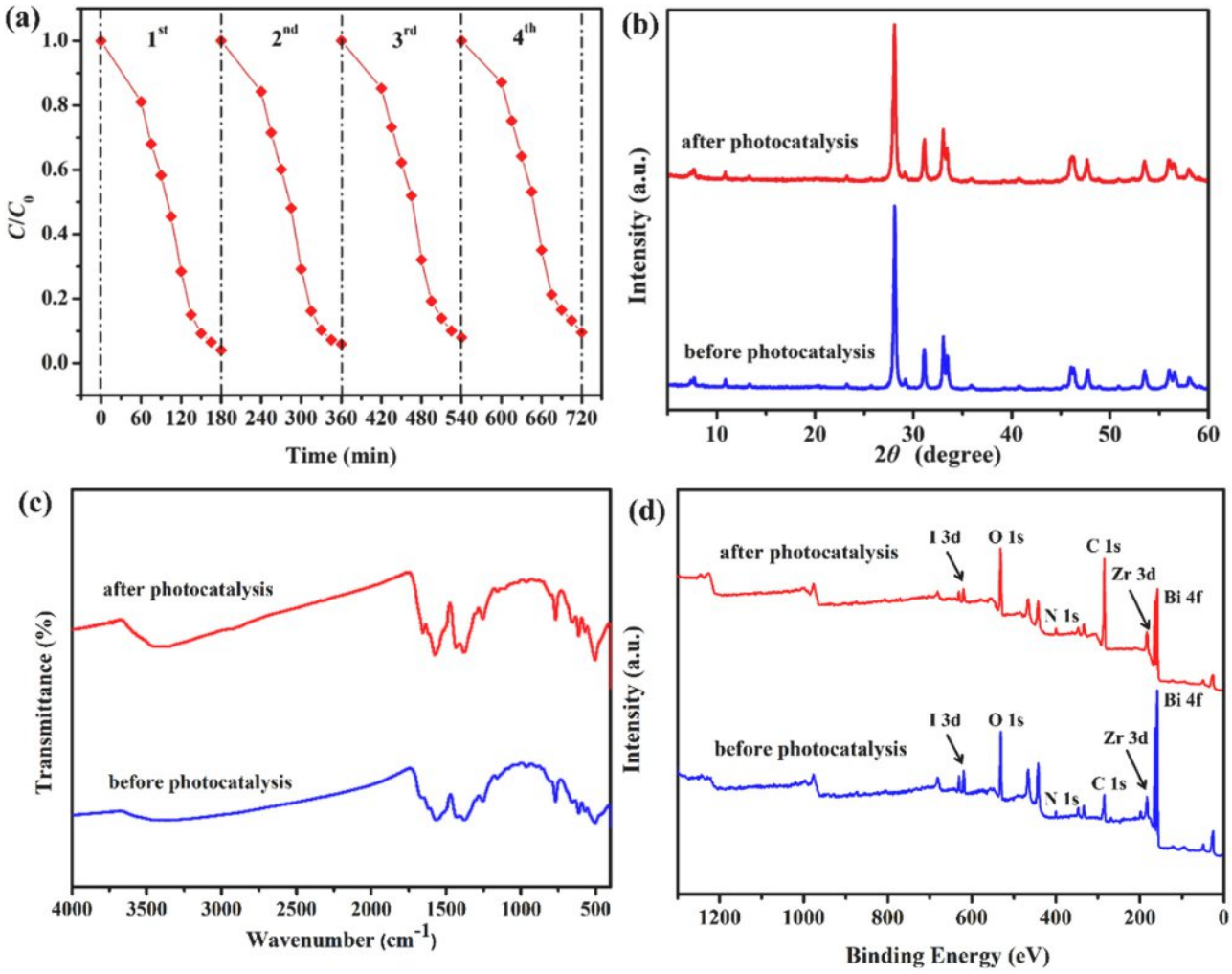

Fig. 10. (a) Cycling experiment for the CIP removal over the BU-5 under the irradiation of white light and (b) PXRD, FT-IR patterns and XPS survey spectra of the BU-5 before and after the cycling experiment.

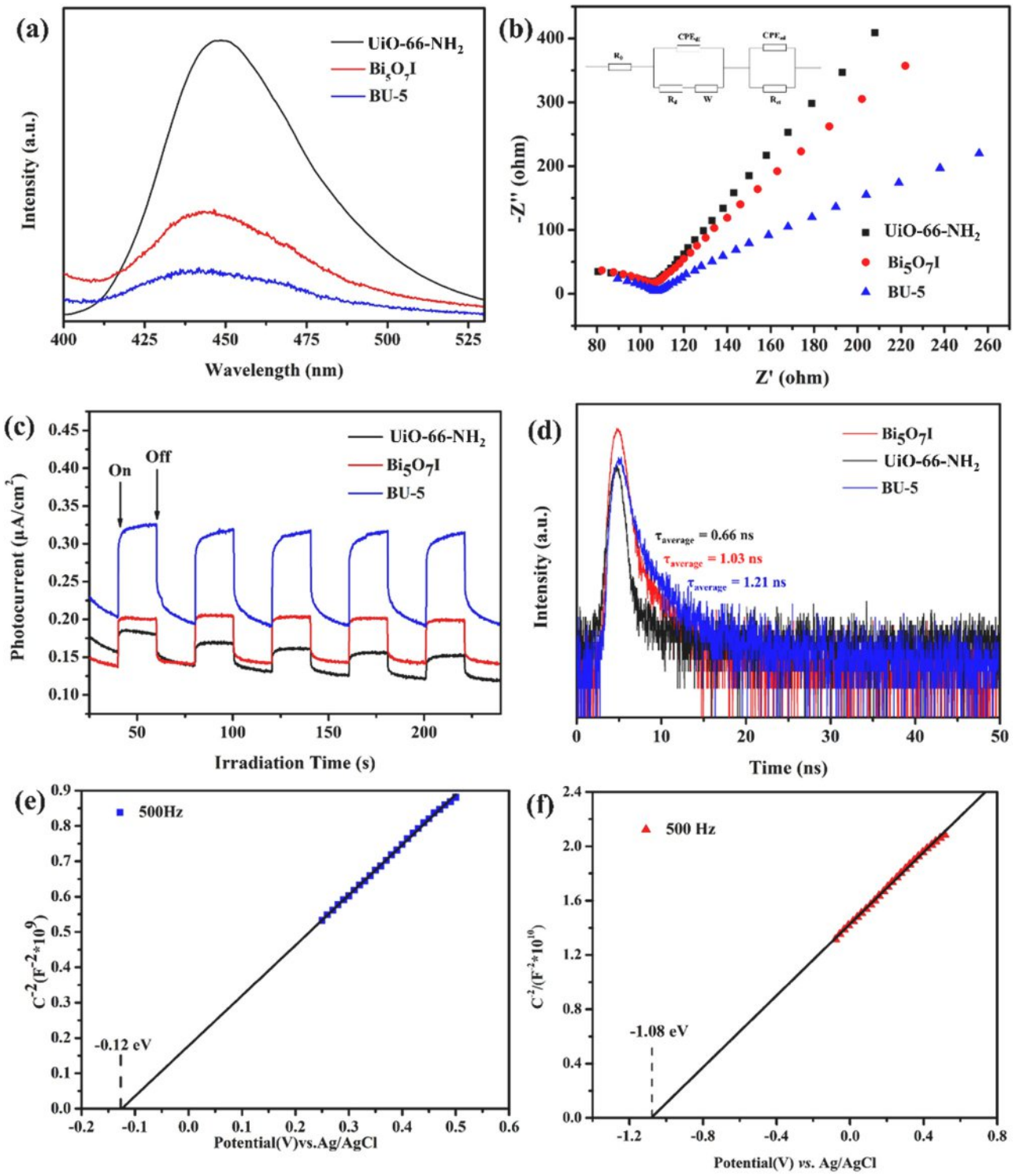

Fig. 11. (a) Steady-state PL spectra, (b) EIS Nyquist plots (c) photocurrent response densities and (d) time-resolved PL decay spectra of UiO-66-NH_2, Bi_5O_7I and BU-5 heterojunction. Mott-Schottky curves of (e) Bi_5O_7I and (f) UiO-66-NH_2 at 500 Hz.

the Mott-Schottky curves of pristine Bi_5O_7I and UiO-66-NH_2 are depicted in Fig. 11(e)-(f). The flat band potentials (E_{FB}) of Bi_5O_7I and UiO-66-NH_2 were calculated to be − 0.12 eV and − 1.08 eV vs. Ag/AgCl electrode, respectively. Additionally, the positive slopes were obtained from the linear C^{-2} potential curve of Bi_5O_7I and UiO-66-NH_2, suggesting that they all behaved n-typed semiconductor properties (Sun et al., 2006). Previous studies had proved that the E_{FB} potential was more positive 0.1 eV than the conduction band potential (E_{CB}) for the most of n-typed semiconductors (Zhao et al., 2020a, 2021b). Therefore, the E_{CB} of Bi_5O_7I and E_{LUMO} of UiO-66-NH_2 were − 0.02 eV and − 0.98 eV vs. NHE. In term of the empirical formula of $E_g = E_{VB} - E_{CB}$, the E_{VB} of Bi_5O_7I and E_{HOMO} of UiO-66-NH_2 were equivalent to 2.96 eV and 1.96 eV vs. NHE.

The trapping experiment was conducted to ascertain the active free radicals involved in the CIP degradation. Various scavengers like p-benzoquinone (BQ), tert-butyl alcohol (TBA) and potassium iodide (KI)

were introduced into the photocatalytic reactor to capture $\cdot O_2^-$, ·OH and h^+, respectively (Zhao et al., 2018c; Ji et al., 2020). Fig. S7 showed that upon using BQ a clear inhibitory effect on the CIP degradation was observed, the corresponding photocatalytic efficiency decreased to 46.5%, manifesting that $\cdot O_2^-$ was the dominating active species in CIP degradation process. Additionally, the incorporation of KI caused a significant reduction of the BU-5′s activity (only 65.5%), suggesting that h^+ played the second role for CIP decomposition in this photocatalytic reaction system. On one hand, h^+ might directly oxidize the CIP molecules in aqueous solution. On the other hand, h^+ can react with H_2O to produce ·OH, which is involved in the removal of CIP. Meanwhile, the addition of TPA reduced the photocatalytic efficiency by 25.3%, revealing that ·OH also participated the CIP degradation process under white light irradiation.

The existence of active species during the photocatalytic process was further validated by performing ESR technique. As depicted in Fig. S8, the significant peaks with $g = 2.004$ can be detected in UiO-66-NH_2, Bi_5O_7I and BU-5, which should be attributed to the trapping h^+ centers on the materials' surface (Ji et al., 2020). Additionally, it was obvious that the signal for h^+ in the BU-5 was much stronger than those of pristine UiO-66-NH_2 and Bi_5O_7I, revealing that much more h^+ will be generated during photocatalytic process and the h^+-induced radical like ·OH might enhance the CIP photodegradation. Furthermore, ESR was also used to trap ·OH and $\cdot O_2^-$ radicals. As illustrated in Fig. 12, strong DMPO-·O_2^- signals and negligible DMPO-·OH signal were observed over UiO-66-NH_2 under white light irradiation, indicating that $\cdot O_2^-$ radicals were preferably produced for UiO-66-NH_2 upon photo-excitation process. On the contrary, obvious DMPO-·OH signals were detected in the ESR spectra of Bi_5O_7I, while no DMPO-·O_2^- signal can be recorded in its corresponding ESR spectra. However, being compared with pristine UiO-66-NH_2 and Bi_5O_7I, both the DMPO-·OH and DMPO-·O_2^- signals appeared in the ESR spectra of BU-5. Based on the above results, a reasonable mechanism for CIP degradation is proposed in Fig. 13. As for the Bi_5O_7I/UiO-66-NH_2 heterojunction constructed in the current work, if a conventional type II heterojunction was formed under white light illumination, then the photo-generated electrons undergo migration from the LUMO of UiO-66-NH_2 to the CB of Bi_5O_7I, whereas transport of holes occurred from the VB of Bi_5O_7I to HOMO of UiO-66-NH_2. Such charge transfer configuration was bound to weak oxidation ability of the holes and decrease reduction ability of the electrons. More importantly, the CB accumulated electrons of Bi_5O_7I and the holes occupying HOMO of UiO-66-NH_2 cannot reduce O_2 to form $\cdot O_2^-$ and oxidize H_2O to produce ·OH owing to the thermodynamic restriction. Based on the aforementioned results, a Z-scheme charge transfer process is an excellent approach to understand the improved photocatalytic efficiency of the BU-*x* heterojunctions. Under white light exposure, the photo-generated electrons in the CB of Bi_5O_7I were inclined to be transferred into the HOMO of UiO-66-NH_2 due to strong electrostatic attraction between the electrons in CB of Bi_5O_7I and holes in HOMO of UiO-66-NH_2. In that way, the space separation of photo-generated electron-hole pairs can be remarkably improved within UiO-66-NH_2 and Bi_5O_7I. Therefore, the electrons retained in the LUMO of UiO-66-NH_2 were more susceptible to be trapped by O_2 to form $\cdot O_2^-$ because of more negative E_{LUMO} of UiO-66-NH_2 (− 0.98 eV vs. NHE) than the standard redox potential of $O_2/\cdot O_2^-$ (− 0.33 eV vs. NHE) (Zhao et al., 2020a; Yi et al., 2019; Chen et al., 2020). Additionally, the holes in the VB of Bi_5O_7I can react with H_2O to generate ·OH because the E_{VB} of Bi_5O_7I (2.96 eV vs. NHE) was more positive compare with standard redox potential of $H_2O/\cdot OH$ (2.40 eV vs. NHE) (Zhao et al., 2021b, 2020b; Chen et al., 2020). Thus, the generated $\cdot O_2^-$ and ·OH subsequently took part in the CIP degradation process. Previous studies suggested that the Pt nanoparticles could be reduced from H_2PtCl_6 via accepting the photo-generated electrons, thus it can be used to confirm the charge transfer route from the other perspective (Wang et al., 2021; Yi et al., 2021). As shown in Fig. 14(a), it can be observed that the Pt nanoparticles were mainly deposited around the UiO-66-NH_2 octahedron, indicating that the BU-5 followed the Z-scheme charge transfer process. Additionally, the charge transfer mechanism between UiO-66-NH_2 and Bi_5O_7I was verified by Bader charge simulating computation. The optimized structure model of the Bi_5O_7I/UiO-66-NH_2 heterojunction and the result of Bader charge analysis were shown in Fig. 14(b) and Table S2, respectively. The results revealed that average 0.2026 electrons migrated from Bi_5O_7I to UiO-66-NH_2 at the Bi_5O_7I/UiO-66-NH_2 interface. Accumulation of net charges was contributed to generate a built-in electric field at the interface (Singh et al., 2020; Liu, 2015), which involved to suppress the recombination of electron-hole pairs and increase the probability of

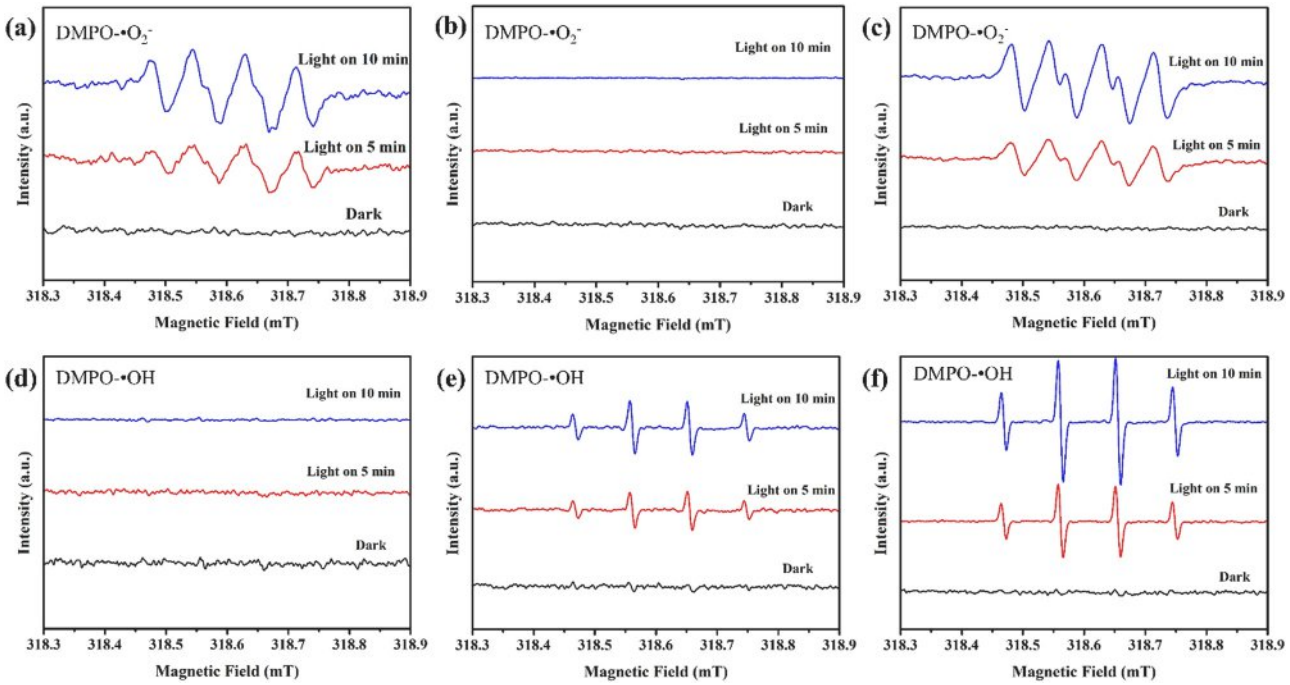

Fig. 12. DMPO-·OH and DMPO-·O_2^- signals of (a, d) NH_2-UiO-66, (b, e) Bi_5O_7I and (c, f) BU-5 samples.

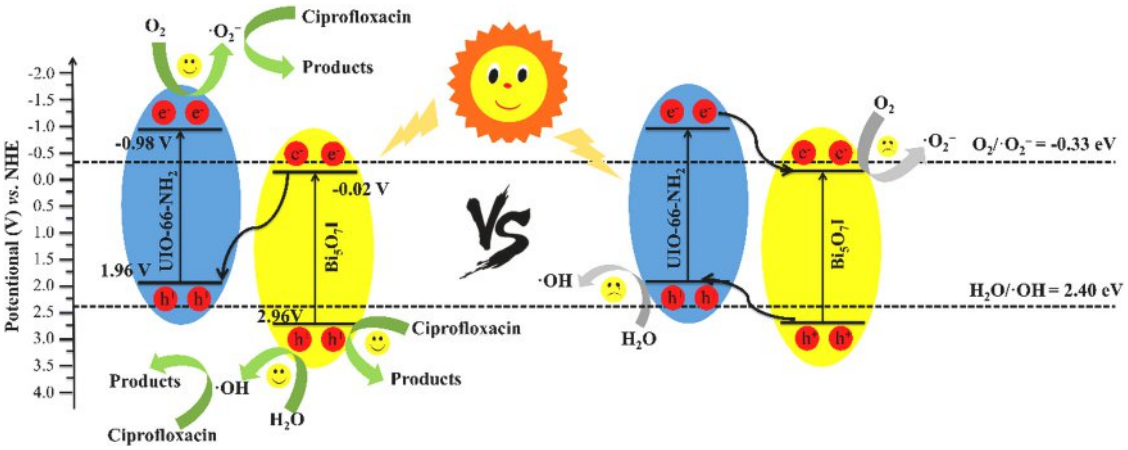

Fig. 13. The possible mechanism for CIP degradation over the UiO-66-NH_2/Bi_5O_7I heterojunctions under white light irradiation.

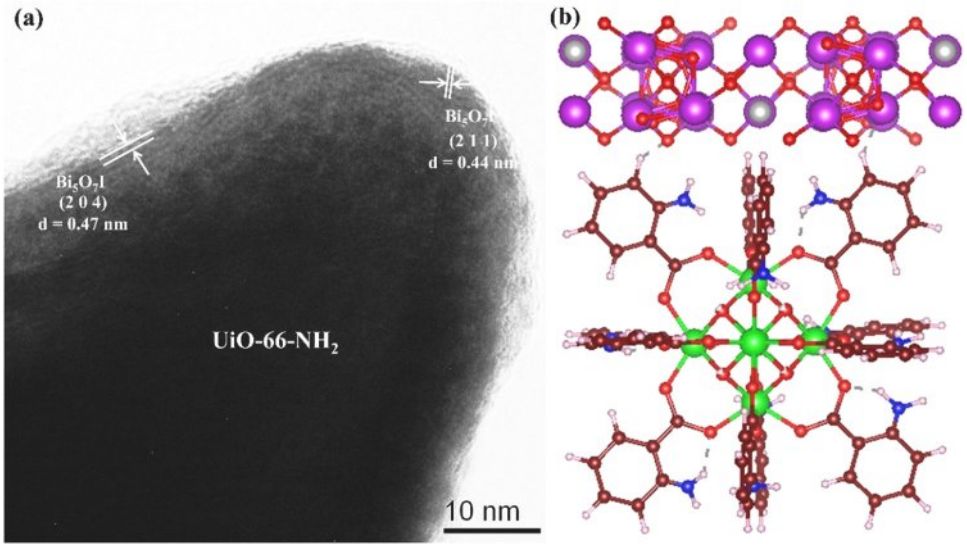

Fig. 14. (a) HRTEM image of photo-deposited Pt nanoparticles over the BU-5 and (b) optimized structure model of the Bi_5O_7I/UiO-66-NH_2 heterojunction. The brown, blue, red, pink, green, purple, and grey spheres represent the C, N, O, H, Zr, Bi and I atoms, respectively. (For interpretation of the references to colour in this figure legend, the reader is referred to the web version of this article.)

charge carriers participating in the redox reactions on the surface of UiO-66-NH_2/Bi_5O_7I heterojunction. Therefore, the DFT calculation results were consistent with the experimental results and proved the formation of Z-scheme heterojunction between the UiO-66-NH_2 and Bi_5O_7I.

3.5. Evaluation of degradation pathway and toxicity

The intermediate products of CIP by BU-5 were detected by UPLC-Q-TOF-MS to deduce the degradation pathway. During the photocatalytic process, eleven intermediates were spotted with *m/z* of 362, 306, 291, 263, 245, 334, 348, 278, 288 and 243. As illustrated in Fig. 15, the CIP photodegradation mainly underwent three pathways, including the degradation of piperazine ring and the breaking of quinolone moiety. To be more specific, the first decomposition step of CIP was the oxidation and breakage of piperazine ring to generate product A (pathway 1). Then the product B was produced by losing two groups of C═O and the intermediate B could be converted into C simultaneously via the process of hydroxylation and losing of CH–NH_2 group. Moreover, under the action of h^+, the intermediates F and G were created via a release of C═O group. It was worth noting that the generated G can also be converted into C via oxidation of $\cdot O_2^-$ and ·OH radicals. The formation of product D was associated with the removal of C═O from product C, which was then converted into intermediate E via the process of defluorination with the aid of h^+ attack and illumination of white light (Salma et al., 2016). Yu and co-workers (Yu et al., 2019) had applied the theoretical calculation of the frontier electron densities (FEDs) to reveal that N atom in piperazine ring and C atom attached to carboxyl group were easily attacked by ·OH. Because the N atom possessed greater steric hindrance, hence the C atom within the quinolone structure was attacked by ·OH and induced the production of intermediate J via the process of decarboxylation (pathway 2). Afterward, the piperazine and adjacent C═C in quinolone structure of intermediate J could be further oxidized and allowed the formation of intermediate K. Such degradation pathway was found in FeS_2/SiO_2 and Zn-doped Cu_2O catalytic systems (Yu et al., 2019; Diao et al., 2017). With respect to pathway 3, the intermediate H was generated from the hydroxylation of CIP. Various reported studies showed the h^+ promoted stepwise oxidation of the piperazine side chain (Xu et al., 2019; Lai et al., 2019; Yu et al., 2019; Hu et al., 2020b) and the oxidizability of functional groups followed the order of pyridone ring < phenyl ring < piperazine ring (Sturini et al., 2010). Therefore, the intermediate I was preferentially created via dealkylation and hydroxyl group substitution. More importantly, the above active species could persistently act on CIP degradation process, which resulted in the mineralization of the above unstable intermediates

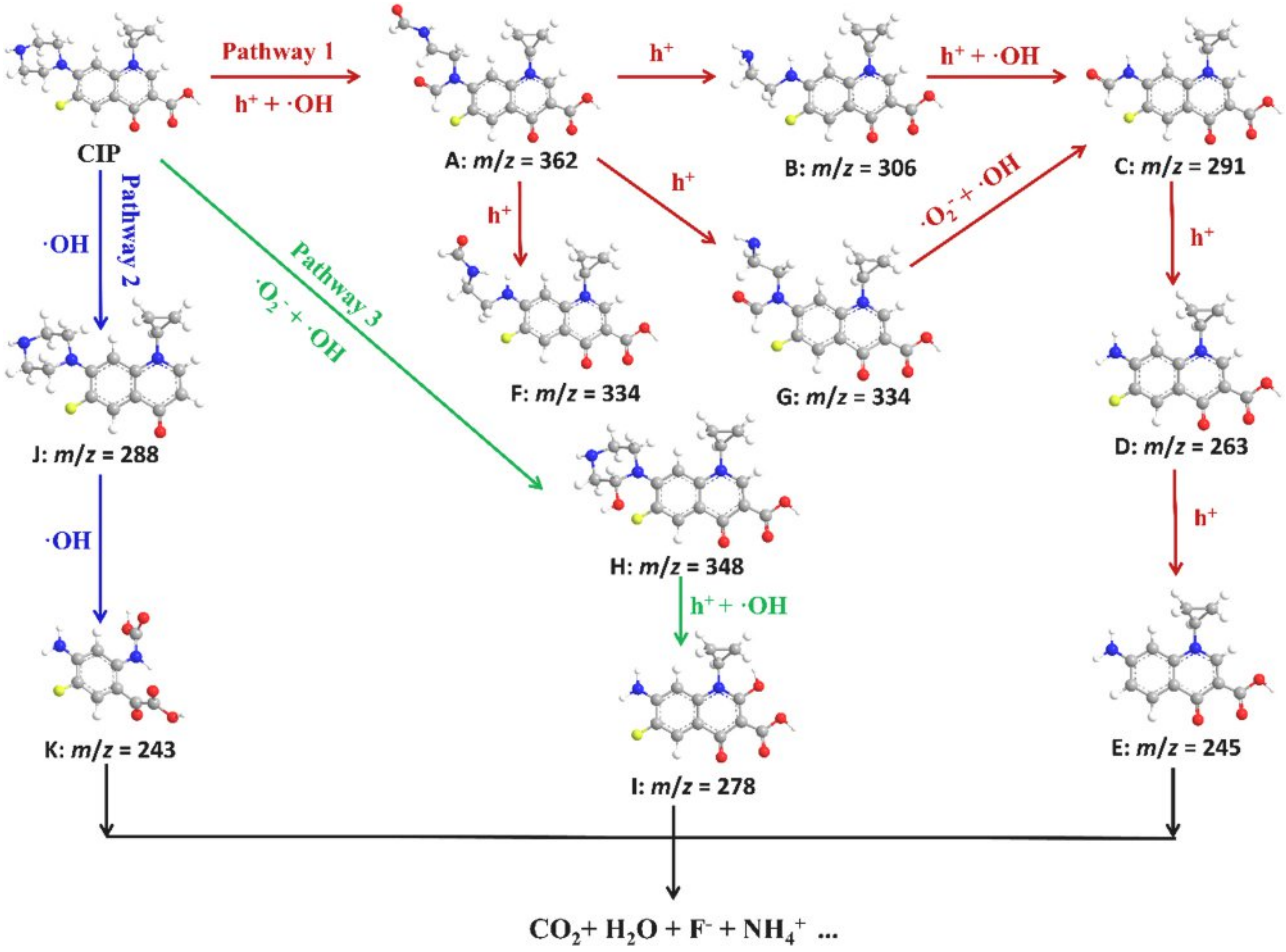

Fig. 15. Possible photocatalytic pathways of CIP by BU-5 heterojunction under white light irradiation.

into F^-, NH_4^+, CO_2 and H_2O. Fig. S9 exhibited the accumulation curves of inorganic ions at pre-set time intervals. It was observed that the concentrations of F^- and NH_4^+ were increased gradually during the photocatalysis. Agreement with the proposed three pathways, the F^- was derived from the cleavage of C–F bond and NH_4^+ resulted from the breakage of C–N bond in piperazine ring.

The toxicity of CIP and its degradation intermediates were studied with the help of Toxicity Estimation Software TOOL (T.E.S.T.) (Ji et al., 2020; Chen et al., 2021b; Cai et al., 2019). Four indexes including *Daphnia magna* LC_{50}, mutagenicity, bioaccumulation factor and developmental toxicity were predicted according to the quantitative structure-activity relationship (QSAR) method. For the acute toxicity, CIP with a *Daphnia magna* LC_{50} value of 0.11 mg/L was recognized as "toxic" (Fig. S10(a)). However, after the photocatalytic treatment, all the intermediates displayed higher LC_{50} values, indicating the acute toxicity was reduced. Fig. S10(b) showed that the Bi_5O_7I/UiO-66-NH_2 photocatalytic system can significantly reduce the mutagenicity toxicity. Most of intermediates (compounds C, E, F, G, I and K) were transformed into "mutagenicity negative". Similarly, almost all the intermediates (except for compound J) showed lower bioaccumulation factor (Fig. S10 (c)), indicating the rupture of piperazine moiety could proceed through the loss of toxicity. Furthermore, CIP with a developmental toxicity index of 0.97 was considered as a "developmental toxicant". Nevertheless, most of intermediates exhibited lower developmental toxicity (Fig. S10(d)). Based on the above analysis, the constructed Bi_5O_7-I/UiO-66-NH_2 photocatalytic process was a "green" methodology owing to the toxicity attenuation performance, indicating great practical potential in treatment of CIP-containing wastewater.

4. Conclusions

In summary, novel Bi_5O_7I/UiO-66-NH_2 heterostructured photocatalysts were fabricated through a facile ball-milling method. The as-prepared BU-5 photocatalyst showed a remarkable performance for the CIP degradation under the irradiation of white light comparing with pristine UiO-66-NH_2 and Bi_5O_7I. The presence of UiO-66-NH_2 could enlarge the surface area of BU-*x* materials, thereby improving the adsorption capacity and providing abundant photocatalytic active sites for decomposing organic pollutants. Based on the capture experiment of active radicals, Mott-Schottky measurements, ESR signals and DFT simulation, the Bi_5O_7I/UiO-66-NH_2 heterostructures followed the mechanism of direct Z-scheme charge transfer rather than a conventional type II heterojunction charge transfer mechanism. In that way, the CB electrons of Bi_5O_7I were combined with the holes in HOMO of UiO-66-NH_2 and resulted in enhanced migration and utilization of charge carriers via photo-excitation process. Moreover, the acute toxicity of many intermediates was decreased during the photocatalytic process, revealing that the great potential for practical application of BU-*x* heterojunctions in further quinolone antibiotics wastewater treatment. Meanwhile, this work provides an effective approach to construct direct Z-scheme bismuth-rich bismuth oxyhalide/MOF heterostructured photocatalysts.

CRediT authorship contribution statement

Chen Zhao: Data curation, Investigation, Visualization, Writing - original draft preparation. **Yang Li**: Resources, Software, Validation. **Hongyu Chu**: Investigation, Instrumental. **Xi Pan**: Resources,

Instrumental. **Li Ling**: Resources, Instrumental. **Peng Wang**: Instrumental. **Huifen Fu**: Resources, Validation. **Chong-Chen Wang**: Conceptualization, Funding acquisition, Supervision, Project administration, Writing - review & editing. **Zhihua Wang**: Funding acquisition, Supervision, Project administration.

Declaration of Competing Interest

The authors declare that they have no known competing financial interests or personal relationships that could have appeared to influence the work reported in this paper.

Acknowledgements

This work was supported by National Natural Science Foundation of China (51878023 and 21876008), Beijing Natural Science Foundation (8202016), Great Wall Scholars Training Program Project of Beijing Municipality Universities (CIT&TCD20180323), Beijing Talent Project (2020A27), Science and Technology General Project of Beijing Municipal Education Commission (KM202110016010) and The Fundamental Research Funds for Beijing University of Civil Engineering and Architecture (X20147/X20141/X20135/X20146).

Appendix A. Supporting information

Supplementary data associated with this article can be found in the online version at doi:10.1016/j.jhazmat.2021.126466.

References

Agrawal, N., Ray, R.S., Farooq, M., Pant, A.B., Hans, R.K., 2007. Photosensitizing potential of ciprofloxacin at ambient level of UV radiation. Photochem. Photobiol. 83, 1226–1236.

Cai, Z., Hao, X., Sun, X., Du, P., Liu, W., Fu, J., 2019. Highly active WO_3@anatase-SiO_2 aerogel for solar-light-driven phenanthrene degradation: mechanism insight and toxicity assessment. Water Res. 162, 369–382.

Chen, D.-D., Yi, X.-H., Zhao, C., Fu, H., Wang, P., Wang, C.-C., 2020. Polyaniline modified MIL-100(Fe) for enhanced photocatalytic Cr(VI) reduction and tetracycline degradation under white light. Chemosphere 245, 125659.

Chen, F., Yang, Q., Yao, F., Wang, S., Sun, J., An, H., Yi, K., Wang, Y., Zhou, Y., Wang, L., Li, X., Wang, D., Zeng, G., 2017. Visible-light photocatalytic degradation of multiple antibiotics by AgI nanoparticle-sensitized Bi_5O_7I microspheres: Enhanced interfacial charge transfer based on Z-scheme heterojunctions. J. Catal. 352, 160–170.

Chen, G., Yu, Y., Liang, L., Duan, X., Li, R., Lu, X., Yan, B., Li, N., Wang, S., 2021a. Remediation of antibiotic wastewater by coupled photocatalytic and persulfate oxidation system: a critical review. J. Hazard. Mater. 408, 124461.

Chen, L., Ji, H., Qi, J., Huang, T., Wang, C.-C., Liu, W., 2021b. Degradation of acetaminophen by activated peroxymonosulfate using $Co(OH)_2$ hollow microsphere supported titanate nanotubes: insights into sulfate radical production pathway through $CoOH^+$ activation. Chem. Eng. J. 406, 126877.

Chen, M., Yao, J., Huang, Y., Gong, H., Chu, W., 2018a. Enhanced photocatalytic degradation of ciprofloxacin over Bi_2O_3/$(BiO)_2CO_3$ heterojunctions: efficiency, kinetics, pathways, mechanisms and toxicity evaluation. Chem. Eng. J. 334, 453–461.

Chen, R., Chen, Z., Ji, M., Chen, H., Liu, Y., Xia, J., Li, H., 2018b. Enhanced reactive oxygen species activation for building carbon quantum dots modified Bi_5O_7I nanorod composites and optimized visible-light-response photocatalytic performance. J. Colloid Interface Sci. 532, 727–737.

Cheng, H., Wu, J., Tian, F., Liu, Q., Qi, X., Li, Q., Pan, W., Li, Z., Wei, J., 2019. Visible-light photocatalytic oxidation of gas-phase Hg^0 by colored TiO_2 nanoparticle-sensitized Bi_5O_7I nanorods: enhanced interfacial charge transfer based on heterojunction. Chem. Eng. J. 360, 951–963.

Di, J., Xia, J., Ji, M., Yin, S., Li, H., Xu, H., Zhang, Q., Li, H., 2015. Controllable synthesis of $Bi_4O_5Br_2$ ultrathin nanosheets for photocatalytic removal of ciprofloxacin and mechanism insight. J. Mater. Chem. A 3, 15108–15118.

Diao, Z.-H., Xu, X.-R., Jiang, D., Li, G., Liu, J.-J., Kong, L.-J., Zuo, L.-Z., 2017. Enhanced catalytic degradation of ciprofloxacin with FeS_2/SiO_2 microspheres as heterogeneous Fenton catalyst: kinetics, reaction pathways and mechanism. J. Hazard. Mater. 327, 108–115.

Ding, J., Yang, Z., He, C., Tong, X., Li, Y., Niu, X., Zhang, H., 2017. UiO-66(Zr) coupled with Bi_2MoO_6 as photocatalyst for visible-light promoted dye degradation. J. Colloid Interface Sci. 497, 126–133.

Dodd, M.C., Shah, A.D., von Gunten, U., Huang, C.-H., 2005. Interactions of fluoroquinolone antibacterial agents with aqueous chlorine: reaction kinetics, mechanisms, and transformation pathways. Environ. Sci. Technol. 39, 7065–7076.

Gad-Allah, T.A., Ali, M.E.M., Badawy, M.I., 2011. Photocatalytic oxidation of ciprofloxacin under simulated sunlight. J. Hazard. Mater. 186, 751–755.

Geng, X., Chen, S., Lv, X., Jiang, W., Wang, T., 2018. Synthesis of g-C_3N_4/Bi_5O_7I microspheres with enhanced photocatalytic activity under visible light. Appl. Surf. Sci. 462, 18–28.

Guo, H.-G., Gao, N.-Y., Chu, W.-H., Li, L., Zhang, Y.-J., Gu, J.-S., Gu, Y.-L., 2013. Photochemical degradation of ciprofloxacin in UV and UV/H_2O_2 process: kinetics, parameters, and products. Environ. Sci. Pollut. Res. 20, 3202–3213.

Hu, K., Li, R., Ye, C., Wang, A., Wei, W., Hu, D., Qiu, R., Yan, K., 2020a. Facile synthesis of Z-scheme composite of TiO_2 nanorod/g-C_3N_4 nanosheet efficient for photocatalytic degradation of ciprofloxacin. J. Clean. Prod. 253, 120055.

Hu, Q., Chen, Y., Li, M., Zhang, Y., Wang, B., Zhao, Y., Xia, J., Yin, S., Li, H., 2019. Construction of NH_2-UiO-66/BiOBr composites with boosted photocatalytic activity for the removal of contaminants. Colloids Surf. A Physicochem. Eng. Asp. 579, 123625.

Hu, X., Hu, X., Peng, Q., Zhou, L., Tan, X., Jiang, L., Tang, C., Wang, H., Liu, S., Wang, Y., Ning, Z., 2020b. Mechanisms underlying the photocatalytic degradation pathway of ciprofloxacin with heterogeneous TiO_2. Chem. Eng. J. 380, 122366.

Iqbal, P., Critchley, K., Attwood, D., Tunnicliffe, D., Evans, S.D., Preece, J.A., 2008. Chemical manipulation by X-rays of functionalized thiolate self-assembled monolayers on Au. Langmuir 24, 13969–13976.

Jahurul Islam, M., Kim, H.K., Amaranatha Reddy, D., Kim, Y., Ma, R., Baek, H., Kim, J., Kim, T.K., 2017. Hierarchical BiOI nanostructures supported on a metal organic framework as efficient photocatalysts for degradation of organic pollutants in water. Dalton Trans. 46, 6013–6023.

Ji, H., Du, P., Zhao, D., Li, S., Sun, F., Duin, E.C., Liu, W., 2020. 2D/1D graphitic carbon nitride/titanate nanotubes heterostructure for efficient photocatalysis of sulfamethazine under solar light: catalytic "hot spots" at the rutile–anatase–titanate interfaces. Appl. Catal. B Environ. 263, 118357.

Jin, X., Ye, L., Xie, H., Chen, G., 2017. Bismuth-rich bismuth oxyhalides for environmental and energy photocatalysis. Coord. Chem. Rev. 349, 84–101.

Kardanpour, R., Tangestaninejad, S., Mirkhani, V., Moghadam, M., Mohammadpoor-Baltork, I., Zadehahmadi, F., 2015. Efficient alkene epoxidation catalyzed by molybdenyl acetylacetonate supported on aminated UiO-66 metal−organic framework. J. Solid State Chem. 226, 262–272.

Kovalakova, P., Cizmas, L., McDonald, T.J., Marsalek, B., Feng, M., Sharma, V.K., 2020. Occurrence and toxicity of antibiotics in the aquatic environment: a review. Chemosphere 251, 126351.

Kresse, G., Furthmüller, J., 1996a. Efficient iterative schemes for ab initio total-energy calculations using a plane-wave basis set. Phys. Rev. B 54, 11169–11186.

Kresse, G., Furthmüller, J., 1996b. Efficiency of ab-initio total energy calculations for metals and semiconductors using a plane-wave basis set, Comp. Mater. Sci. 6, 15–50.

Lai, C., Zhang, M., Li, B., Huang, D., Zeng, G., Qin, L., Liu, X., Yi, H., Cheng, M., Li, L., Chen, Z., Chen, L., 2019. Fabrication of CuS/$BiVO_4$ (0 4 0) binary heterojunction photocatalysts with enhanced photocatalytic activity for Ciprofloxacin degradation and mechanism insight. Chem. Eng. J. 358, 891–902.

Li, G., Huang, Y., Lin, J., Yu, C., Liu, Z., Fang, Y., Xue, Y., Tang, C., 2020a. Effective capture and reversible storage of iodine using foam-like adsorbents consisting of porous boron nitride microfibers. Chem. Eng. J. 382, 122833.

Li, S., Huang, T., Du, P., Liu, W., Hu, J., 2020b. Photocatalytic transformation fate and toxicity of ciprofloxacin related to dissociation species: experimental and theoretical evidences. Water Res. 185, 116286.

Li, Y.-X., Wang, X., Wang, C.-C., Fu, H., Liu, Y., Wang, P., Zhao, C., 2020c. S-TiO_2/UiO-66-NH_2 composite for boosted photocatalytic Cr(VI) reduction and bisphenol A degradation under LED visible light. J. Hazard. Mater. 399, 123085.

Li, Z., Dong, H., Wu, Z., Shen, J., Xu, D., He, R., Wan, L., Zhang, S., 2020d. Novel p-n type porous Ag_2O/Bi_5O_7I heterojunction for Uv–Vis-NIR activated high efficient photocatalytic degradation of bisphenol A: photoelectric properties and degradation mechanism. Appl. Surf. Sci. 529, 147162.

Liang, C., Niu, C.-G., Zhang, L., Wen, X.-J., Yang, S.-F., Guo, H., Zeng, G.-M., 2019. Construction of 2D heterojunction system with enhanced photocatalytic performance: plasmonic Bi and reduced graphene oxide co-modified Bi_5O_7I with high-speed charge transfer channels. J. Hazard. Mater. 361, 245–258.

Liao, C.-H., Kang, S.-F., Wu, F.-A., 2001. Hydroxyl radical scavenging role of chloride and bicarbonate ions in the H_2O_2/UV process. Chemosphere 44, 1193–1200.

Liao, G., Li, C., Li, X., Fang, B., 2021. Emerging polymeric carbon nitride Z-scheme systems for photocatalysis. Cell Rep. Phys. Sci. 2, 100355.

Lin, K.-Y.A., Chen, S.-Y., Jochems, A.P., 2015. Zirconium-based metal organic frameworks: highly selective adsorbents for removal of phosphate from water and urine. Mater. Chem. Phys. 160, 168–176.

Liu, C., Huang, H., Du, X., Zhang, T., Tian, N., Guo, Y., Zhang, Y., 2015. In situ co-crystallization for fabrication of g-C_3N_4/Bi_5O_7I heterojunction for enhanced visible-light photocatalysis. J. Phys. Chem. C 119, 17156–17165.

Liu, J., 2015. Origin of high photocatalytic efficiency in monolayer g-C_3N_4/CdS heterostructure: a hybrid DFT study. J. Phys. Chem. C 119, 28417–28423.

Liu, N., Lu, N., Su, Y., Wang, P., Quan, X., 2019. Fabrication of g-C_3N_4/Ti_3C_2 composite and its visible-light photocatalytic capability for ciprofloxacin degradation. Sep. Purif. Technol. 211, 782–789.

Liu, Y., He, X., Fu, Y., Dionysiou, D.D., 2016. Degradation kinetics and mechanism of oxytetracycline by hydroxyl radical-based advanced oxidation processes. Chem. Eng. J. 284, 1317–1327.

Low, J., Jiang, C., Cheng, B., Wageh, S., Al-Ghamdi, A.A., Yu, J., 2017. A review of direct Z-Scheme photocatalysts. Small Methods 1, 1700080.

Lu, N., Wang, P., Su, Y., Yu, H., Liu, N., Quan, X., 2019. Construction of Z-Scheme g-C_3N_4/RGO/WO_3 with in situ photoreduced graphene oxide as electron mediator for efficient photocatalytic degradation of ciprofloxacin. Chemosphere 215, 444–453.

Ma, Y., Chen, Z., Qu, D., Shi, J., 2016. Synthesis of chemically bonded BiOCl@Bi_2WO_6 microspheres with exposed (020) Bi_2WO_6 facets and their enhanced photocatalytic activities under visible light irradiation. Appl. Surf. Sci. 361, 63–71.
Maimaitizi, H., Abulizi, A., Kadeer, K., Talifu, D., Tursun, Y., 2020. In situ synthesis of Pt and N co-doped hollow hierarchical BiOCl microsphere as an efficient photocatalyst for organic pollutant degradation and photocatalytic CO_2 reduction. Appl. Surf. Sci. 502, 144083.
Mei, F., Zhang, J., Dai, K., Zhu, G., Liang, C., Z-scheme, A., 2019. Bi_2MoO_6/CdSe-diethylenetriamine heterojunction for enhancing photocatalytic hydrogen production activity under visible light. Dalton Trans. 48, 1067–1074.
Mi, Y., Wang, J., Yang, Z., Wang, Z., Wang, H., Yang, S., 2014. A simple one-step solution deposition process for constructing high-performance amorphous zirconium oxide thin film. RSC Adv. 4, 6060–6067.
Mu, X., Jiang, J., Chao, F., Lou, Y., Chen, J., 2018. Ligand modification of UiO-66 with an unusual visible light photocatalytic behavior for RhB degradation. Dalton Trans. 47, 1895–1902.
Phoon, B.L., Ong, C.C., Mohamed Saheed, M.S., Show, P.-L., Chang, J.-S., Ling, T.C., Lam, S.S., Juan, J.C., 2020. Conventional and emerging technologies for removal of antibiotics from wastewater. J. Hazard. Mater. 400, 122961.
Saleh, R., Taufik, A., Prakoso, S.P., 2019. Fabrication of Ag_2O/TiO_2 composites on nanographene platelets for the removal of organic pollutants: influence of oxidants and inorganic anions. Appl. Surf. Sci. 480, 697–708.
Salma, A., Thoröe-Boveleth, S., Schmidt, T.C., Tuerk, J., 2016. Dependence of transformation product formation on pH during photolytic and photocatalytic degradation of ciprofloxacin. J. Hazard. Mater. 313, 49–59.
Santhoshkumar, P., Prasanna, K., Jo, Y.N., Sivagami, I.N., Kang, S.H., Lee, C.W., 2019. Hierarchically structured mesoporous bimetallic oxides as a potential anode material for rechargeable lithium batteries. J. Alloy. Compd. 771, 555–564.
Sarkhosh, M., Sadani, M., Abtahi, M., Mohseni, S.M., Sheikhmohammadi, A., Azarpira, H., Najafpoor, A.A., Atafar, Z., Rezaei, S., Alli, R., Bay, A., 2019. Enhancing photo-degradation of ciprofloxacin using simultaneous usage of eaq− and ·OH over UV/ZnO/I- process: efficiency, kinetics, pathways, and mechanisms. J. Hazard. Mater. 377, 418–426.
Sheng, Y., Yi, D., Qingsong, H., Ting, W., Ming, L., Yong, C., Yifan, S., Jun, D., Bin, W., Xia, J., Huaming, L., 2019. CQDs modified $PbBiO_2Cl$ nanosheets with improved molecular oxygen activation ability for photodegradation of organic contaminants. J. Photochem. Photobiol. A Chem. 382, 111921.
Singh, D., Panda, P.K., Khossossi, N., Mishra, Y.K., Ainane, A., Ahuja, R., 2020. Impact of edge structures on interfacial interactions and efficient visible-light photocatalytic activity of metal–semiconductor hybrid 2D materials. Catal. Sci. Technol. 10, 3279–3289.
Sturini, M., Speltini, A., Maraschi, F., Profumo, A., Pretali, L., Fasani, E., Albini, A., 2010. Photochemical degradation of marbofloxacin and enrofloxacin in natural waters. Environ. Sci. Technol. 44, 4564–4569.
Sun, L.-P., Niu, S.-Y., Jin, J., Yang, G.-D., Ye, L., 2006. Crystal structure and surface photovoltage of a series of Ni(II) coordination supramolecular polymer. Inorg. Chem. Commun. 9, 679–682.
Sun, S., Wang, W., Zhang, L., Zhou, L., Yin, W., Shang, M., 2009. Visible light-induced efficient contaminant removal by Bi_5O_7I. Environ. Sci. Technol. 43, 2005–2010.
Vaiano, V., Iervolino, G., Rizzo, L., 2018. Cu-doped ZnO as efficient photocatalyst for the oxidation of arsenite to arsenate under visible light. Appl. Catal. B Environ. 238, 471–479.
Wang, B., Liu, G., Ye, B., Ye, Y., Zhu, W., Yin, S., Xia, J., Li, H., 2019a. Novel CNT/$PbBiO_2Br$ hybrid materials with enhanced broad spectrum photocatalytic activity toward ciprofloxacin (CIP) degradation. J. Photochem. Photobiol. A Chem. 382, 111901.
Wang, C., Xue, Y., Wang, P., Ao, Y., 2018. Effects of water environmental factors on the photocatalytic degradation of sulfamethoxazole by AgI/UiO-66 composite under visible light irradiation. J. Alloy. Compd. 748, 314–322.
Wang, C.-C., Li, J.-R., Lv, X.-L., Zhang, Y.-Q., Guo, G., 2014. Photocatalytic organic pollutants degradation in metal–organic frameworks. Energy Environ. Sci. 7, 2831–2867.
Wang, C.-C., Du, X.-D., Li, J., Guo, X.-X., Wang, P., Zhang, J., 2016. Photocatalytic Cr(VI) reduction in metal-organic frameworks: a mini-review. Appl. Catal. B Environ. 193, 198–216.
Wang, C.-C., Yi, X.-H., Wang, P., 2019b. Powerful combination of MOFs and C_3N_4 for enhanced photocatalytic performance. Appl. Catal. B Environ. 247, 24–48.
Wang, C.-C., Wang, X., Liu, W., 2020. The synthesis strategies and photocatalytic performances of TiO_2/MOFs composites: a state-of-the-art review. Chem. Eng. J. 391, 123601.
Wang, J.-W., Qiu, F.-G., Wang, P., Ge, C., Wang, C.-C., 2021. Boosted bisphenol A and Cr (VI) cleanup over Z-scheme WO_3/MIL-100(Fe) composites under visible light. J. Clean. Prod. 279, 123408.
Wang, S., Yang, X., Zhang, X., Ding, X., Yang, Z., Dai, K., Chen, H., 2017. A plate-on-plate sandwiched Z-scheme heterojunction photocatalyst: BiOBr-Bi_2MoO_6 with enhanced photocatalytic performance. Appl. Surf. Sci. 391, 194–201.
Wang, Y.R., Chu, W., 2012. Photo-assisted degradation of 2,4,5-trichlorophenoxyacetic acid by Fe(II)-catalyzed activation of Oxone process: the role of UV irradiation, reaction mechanism and mineralization. Appl. Catal. B Environ. 123–124, 151–161.
Wei, Z., Liu, J., Shangguan, W., 2020. A review on photocatalysis in antibiotic wastewater: pollutant degradation and hydrogen production. Chin. J. Catal. 41, 1440–1450.
Wen, X.-J., Niu, C.-G., Zhang, L., Liang, C., Guo, H., Zeng, G.-M., 2018. Photocatalytic degradation of ciprofloxacin by a novel Z-scheme CeO_2–Ag/AgBr photocatalyst: influencing factors, possible degradation pathways, and mechanism insight. J. Catal. 358, 141–154.
Xu, L., Chen, W.-Q., Ke, S.-Q., Zhang, S.-M., Zhu, M., Zhang, Y., Shi, W.-Y., Horike, S., Tang, L., 2020. Construction of heterojunction Bi/Bi_5O_7I/Sn_3O_4 for efficient noble-metal-free Z-scheme photocatalytic H_2 evolution. Chem. Eng. J. 382, 122810.
Xu, X., Ding, X., Yang, X., Wang, P., Li, S., Lu, Z., Chen, H., 2019. Oxygen vacancy boosted photocatalytic decomposition of ciprofloxacin over Bi_2MoO_6: oxygen vacancy engineering, biotoxicity evaluation and mechanism study. J. Hazard. Mater. 364, 691–699.
Xu, X.-Y., Chu, C., Fu, H., Du, X.-D., Wang, P., Zheng, W., Wang, C.-C., 2018. Light-responsive UiO-66-NH_2/Ag_3PO_4 MOF-nanoparticle composites for the capture and release of sulfamethoxazole. Chem. Eng. J. 350, 436–444.
Yang, Z., Tong, X., Feng, J., He, S., Fu, M., Niu, X., Zhang, T., Liang, H., Ding, A., Feng, X., 2019. Flower-like BiOBr/UiO-66-NH_2 nanosphere with improved photocatalytic property for norfloxacin removal. Chemosphere 220, 98–106.
Yi, F., Ma, J., Lin, C., Wang, L., Zhang, H., Qian, Y., Zhang, K., 2020. Insights into the enhanced adsorption/photocatalysis mechanism of a Bi_4O_5Br2/g-C_3N_4 nanosheet. J. Alloy. Compd. 821, 153557.
Yi, X.-H., Ma, S.-Q., Du, X.-D., Zhao, C., Fu, H., Wang, P., Wang, C.-C., 2019. The facile fabrication of 2D/3D Z-scheme g-C_3N_4/UiO-66 heterojunction with enhanced photocatalytic Cr(VI) reduction performance under white light. Chem. Eng. J. 375, 121944.
Yi, X.-H., Ji, H., Wang, C.-C., Li, Y., Li, Y.-H., Zhao, C., Wang, A., Fu, H., Wang, P., Zhao, X., Liu, W., 2021. Photocatalysis-activated SR-AOP over PDINH/MIL-88A(Fe) composites for boosted chloroquine phosphate degradation: performance, mechanism, pathway and DFT calculations. Appl. Catal. B Environ. 293, 120229.
Yin, W., Liu, L., Zhang, H., Tang, S., Chi, R., 2020. A facile solvent-free and one-step route to prepare amino-phosphonic acid functionalized hollow mesoporous silica nanospheres for efficient Gd(III) removal. J. Clean. Prod. 243, 118688.
Yu, X., Zhang, J., Zhang, J., Niu, J., Zhao, J., Wei, Y., Yao, B., 2019. Photocatalytic degradation of ciprofloxacin using Zn-doped Cu_2O particles: analysis of degradation pathways and intermediates. Chem. Eng. J. 374, 316–327.
Zeng, C., Hu, Y., Guo, Y., Zhang, T., Dong, F., Du, X., Zhang, Y., Huang, H., 2016. Achieving tunable photocatalytic activity enhancement by elaborately engineering composition-adjustable polynary heterojunctions photocatalysts. Appl. Catal. B Environ. 194, 62–73.
Zhang, F.-M., Sheng, J.-L., Yang, Z.-D., Sun, X.-J., Tang, H.-L., Lu, M., Dong, H., Shen, F.-C., Liu, J., Lan, Y.-Q., 2018. Rational design of MOF/COF hybrid materials for photocatalytic H_2 evolution in the presence of sacrificial electron donors. Angew. Chem. Int. Ed. 57, 12106–12110.
Zhang, W., Wang, S., Ji, J., Li, Y., Zhang, G., Zhang, F., Fan, X., 2013. Primary and tertiary amines bifunctional graphene oxide for cooperative catalysis. Nanoscale 5, 6030–6033.
Zhao, C., Wang, Z., Wang, C., Li, X., Wang, C.-C., 2018a. Photocatalytic degradation of DOM in urban stormwater runoff with TiO_2 nanoparticles under UV light irradiation: EEM-PARAFAC analysis and influence of co-existing inorganic ions. Environ. Pollut. 243, 177–188.
Zhao, C., Wang, Z., Li, X., Yi, X., Chu, H., Chen, X., Wang, C.-C., 2020a. Facile fabrication of BUC-21/$Bi_{24}O_{31}Br_{10}$ composites for enhanced photocatalytic Cr(VI) reduction under white light. Chem. Eng. J. 389, 123431.
Zhao, C., Wang, Z., Chen, X., Chu, H., Fu, H., Wang, C.-C., 2020b. Robust photocatalytic benzene degradation using mesoporous disk-like N-TiO_2 derived from MIL-125(Ti). Chin. J. Catal. 41, 1186–1197.
Zhao, C., Pan, X., Wang, Z., Wang, C.-C., 2021a. Trichloroethylene dechlorination rates, pathways, and efficiencies of ZVMg/C in aqueous solution. J. Hazard. Mater. 417, 128022.
Zhao, C., Wang, J., Chen, X., Wang, Z., Ji, H., Chen, L., Liu, W., Wang, C.-C., 2021b. Bifunctional $Bi_{12}O_{17}Cl_2$/MIL-100(Fe) composites toward photocatalytic Cr(VI) sequestration and activation of persulfate for bisphenol A degradation. Sci. Total Environ. 752, 141901.
Zhao, H., Yang, X., Xu, R., Li, J., Gao, S., Cao, R., 2018b. CdS/NH_2-UiO-66 hybrid membrane reactors for the efficient photocatalytic conversion of CO_2. J. Mater. Chem. A 6, 20152–20160.
Zhao, X., Du, P., Cai, Z., Wang, T., Fu, J., Liu, W., 2018c. Photocatalysis of bisphenol A by an easy-settling titania/titanate composite: effects of water chemistry factors, degradation pathway and theoretical calculation. Environ. Pollut. 232, 580–590.
Zhou, Y.-C., Xu, X.-Y., Wang, P., Fu, H., Zhao, C., Wang, C.-C., 2019. Facile fabrication and enhanced photocatalytic performance of visible light responsive UiO-66-NH_2/Ag_2CO_3 composite. Chin. J. Catal. 40, 1912–1923.
Zhu, X., Gu, J., Wang, Y., Li, B., Li, Y., Zhao, W., Shi, J., 2014. Inherent anchorages in UiO-66 nanoparticles for efficient capture of alendronate and its mediated release. Chem. Commun. 50, 8779–8782.
Zhu, X.-H., Yang, C.-X., Yan, X.-P., 2018. Metal-organic framework-801 for efficient removal of fluoride from water. Microporous Mesoporous Mater. 259, 163–170.